International Journal for Computational Methods in Engineering Science and Mechanics

ISSN: 1550-2287 (Print) 1550-2295 (Online) Journal homepage: http://www.tandfonline.com/loi/ucme20

Multi-Scale Characterization and Modeling of Ductile Failure in Cast Aluminum Alloys

S. Ghosh , V. Dakshinamurthy , C. Hu & J. Bai

To cite this article: S. Ghosh , V. Dakshinamurthy , C. Hu & J. Bai (2008) Multi-Scale Characterization and Modeling of Ductile Failure in Cast Aluminum Alloys, International Journal for Computational Methods in Engineering Science and Mechanics, 9:1, 25-42, DOI: 10.1080/15502280701752635

To link to this article: http://dx.doi.org/10.1080/15502280701752635

International Journal for Computational Methods in Engineering Science and Mechanics, 9:25–42, 2008

ISSN: 1550–2287 print / 1550–2295 online
DOI: 10.1080/15502280701752635

Multi-Scale Characterization and Modeling of Ductile Failure in Cast Aluminum Alloys

S. Ghosh, V. Dakshinamurthy, C. Hu, and J. Bai
Department of Mechanical Engineering, Ohio State University, Columbus, OH, USA

This paper develops three components contributing to the framework of multi-scale modeling of ductile fracture in aluminum alloys. The first module is morphology-based domain partitioning, which delineates regions of statistical inhomogeneity. The second module is micromechanical analysis with particle fragmentation and matrix cracking. A locally enriched VCFEM or LE-VCFEM is developed to incorporate ductile failure through matrix cracking in the form of void growth and coalescence using a non-local Gurson-Tvergaard-Needleman model. The third module develops a homogenized anisotropic plasticity-damage model for macroscopic analysis. Parameters in this GTN model are calibrated from results of homogenization of microstructural variables of microstructural RVE.

Keywords Multiscale Domain Partitioning, Voronoi Cell FEM, Ductile Failure, Anisotropic GTN Model, Multi-Scale Modeling

1. INTRODUCTION

Many metals and alloys consist of heterogeneities in their microstructure. For example, cast aluminum alloys such as A 319 used in automotive systems contain microstructural heterogeneities in the form of silicon particulates, intermetallics, precipitates and voids. The processing routes affect morphological variations such as irregularities in spatial dispersion including clustering and alignment, or irregularities in phase shapes and sizes. Experimental studies on ductile failure in [1–4] have shown that these morphological variations strongly affect microstructural damage nucleation due to particulate cracking and interfacial decohesion, as well as ductile damage growth by matrix rupture due to void growth and coalescence. Argon [5] has shown that particles in clustered regions have a greater propensity towards cracking than those in regions of dilute concentration, since local stresses increase rapidly with reduced distance between neighboring particles. Experimental work in Caceres et al. [6, 7] has demonstrated that larger and longer particles are more prone to cracking and damage accumulation increases with higher dendrite arm spacing. Consequently, rigorous fundamental studies reflecting the actual microstructural morphologies are required for understanding deformation and failure mechanisms. Modeling these alloys for failure properties like strain to failure, ductility and fracture toughness requires special attention on the microstructural morphology. Various computational models have been proposed for analysis of the mechanical properties and response of multi-phase materials using simplified representations of the microstructural morphology as unit cell models in [8–10]. The predictive capabilities of these models for failure properties in nonuniform microstructures are very limited due to simplification of the critical local features that are critical to failure. A few studies have focused on modeling more realistic representation of microstructures with non-uniform dispersion of heterogeneities [11, 12] by combining digital image processing with microstructure modeling. The microstructure-based Voronoi cell finite element model or VCFEM [11–15] has been shown to offer significant promise in accurate analysis of large microstructural regions with high efficiency.

Modeling these materials requires consideration of large domains with special attention on the microstructural morphology. The concept of multi-scale modeling provides the necessary framework for selective micro-analysis in a very limited region of a macroscopic computational domain as done by Ghosh et al. in [16, 17]. The multiscale models undergo domain partitioning based on the evolution of stresses, strains and/or damage in the microstructure. An optimal domain partitioning can significantly enhance the efficiency of multi-scale computational models by keeping the "zoomed-in" regions of intense micromechanical analysis to a minimum. This paper discusses three important

This work has been supported by the National Science Foundation NSF Div Civil and Mechanical Systems Division through the GOALI grant No. CMS-0308666 (Program director: C. Cooper) and by the Department of Energy Aluminum Visions program through grant No. A5997 (sub contract from Univ. of Illinois). This sponsorship is gratefully acknowledged. Computer support by the Ohio Supercomputer Center through grant PAS813-2 is also gratefully acknowledged.

Address correspondence to S. Ghosh, Department of Mechanical Engineering, Ohio State University, Room W496, Scott Laboratory, 201 West 19th Avenue, Columbus, OH 43210, USA. E-mail: ghosh5@osu.edu

ingredients of multi-scale modeling of ductile failure in heterogeneous cast aluminum alloys. These include: (i) a multi-scale characterization based preprocessor for multi-scale models; (ii) microstructural analysis module for ductile fracture; and (iii) a homogenization based continuum damage mechanics model for ductile materials that can be used in macroscopic analysis modules.

The local morphology in many non-uniform heterogeneous materials may warrant embedding pockets of microstructural regions in an otherwise homogenized domain, even prior to starting the analysis. In a concurrent multi-scale model, it is therefore prudent to partition the initial computational domain based on information of the underlying microstructure, prior to mechanical analysis. The morphology-based domain partitioning (MDP), as a preprocessor to multiscale modeling, is intended for two reasons: (1) to determine microstructural representative volume elements or RVE's that can be used in the "bottom-up" homogenization for different regions in the computational domain; and (2) to identify those regions where the morphology alone (e.g. regions of dense clustering) can cause a breakdown in the homogenization assumption. Embedded regions requiring microstructural analysis should then be coupled with complementary regions of homogenized macroscopic analysis. The MDP process developed in [18, 19] is discussed in detail in section 2.

At the microstructural scale, the complex interaction between competing damage modes in the presence of nonuniformities makes the task of failure analysis rather challenging. Various computational studies have been conducted for understanding the elastic-plastic deformation and damage behavior of discretely reinforced MMC's and other material. Ghosal et al. [20] have studied the fracture initiation around the notch tip, while Steglich et al. [21] have studied the mechanism of void nucleation by debonding or particle cracking. In a comprehensive account of simulation methods for deformation and damage in particle reinforced composites, Llorca [22] has presented investigations on the influence of particle distribution on mechanical properties and ductile failure using multi-particle unit cells. A number of these studies focus on the initial stages of ductile failure and do not consider the effect of microstructural morphology on the evolution of ductile failure by void growth in the matrix and coalescence. In addition, there is a paucity of studies on failure modeling in the presence of multiple reinforcements of different shapes, sizes, orientation and spatial distribution. Ghosh et al. have developed the Voronoi cell finite element model (VCFEM) to simulate particle cracking induced damage [12, 14] and interfacial debonding [11, 15] in particle and fiber reinforced composites with complex non-uniform microstructural morphology. In the present work, the microstructural VCFEM with particle fragmentation is extended to incorporate ductile failure through matrix cracking in the form of void growth and coalescence. Interfacial debonding is not explicitly modeled in this work. However, this occurs by void evolution along the interface between matrix and particle. A non-local Gurson-Tvergaard-Needleman (GTN) model [23–25] is implemented in a locally enriched VCFEM framework or LE-VCFEM for simulating ductile fracture. In LE-VCFEM, the VCFEM formulation is enriched adaptively in narrow bands of localized plastic flow and void growth. In these localized regions, assumed stress hybrid VCFEM formulation is overlaid with a narrow band of displacement based elements to accommodate strain softening.

In the final segment of this paper, an anisotropic continuum damage model for pressure dependent plastic materials is developed for macroscopic analysis in a multi-scale material modeling framework. Damage evolution in ductile materials is inherently a multiple-scale phenomenon where damage initiates at one scale and grows into another. Effective simulators should connect events at different length scales with delineation of morphological details at each scale. It is convenient to use macroscopic constitutive laws obtained by the homogenization of variables obtained from micromechanics simulations. One of the earliest models of anisotropic ductile failure was proposed by Rice [26]. Various continuum constitutive models have been developed based on unit cell analyses of composite and porous microstructures. A number of these models are developed based on the GTN model. Chien et al. [27] have investigated the influence of normal anisotropy of matrix material on the plastic behavior of porous ductile material. Benzerga et al. [28–30] have conducted limit analyses of RVE and incorporated microscopic plastic anisotropy and void shape effect into constitutive equation of porous ductile metal. Most of these models do not consider the complexity of real microstructures and damage interaction. In this paper, an anisotropic GTN type constitutive model is developed for macroscopic damage analysis in particle reinforced aluminum with non-uniform microstructure. The model is based on homogenization of microstructural variables obtained by LE-VCFEM analysis of microstructural representative volume element (RVE) containing particles, matrix and voids. The three modules are detailed in the next sections.

2. MORPHOLOGY BASED DOMAIN PARTITIONING

A necessary requirement of the morphology-based domain partitioning (MDP) process developed in [18, 19] is that accurate information of the microstructural morphology, at least with respect to certain characterization functions, be available at all points of the computational domain. This can be a very challenging and time-consuming task if the entire image has to be acquired by optical or scanning electron microscopy. A few methods have been suggested in the literature for dealing with this problem. A method of preparing a montage of a large number of high magnification microstructural images (nearly 400–500) followed by image compression has been proposed by Gokhale et al. [31, 32]. Their M-SLIP method is effective for small domains where few images are necessary and the microstructural information obtained has been shown to be sufficient for evaluating point statistics in [33]. However, this process of extracting microstructural images at each individual point

may be prohibitively exhaustive for large domains. Alternate statistical methods in the literature include simulated annealing [34, 35], random sequential packing algorithm [35], and Monte-Carlo technique in [36]. All these methods have shortcomings with respect to convergence to the actual image. The MDP process proposed in this study consists of three steps, executed in sequence. They are: (a) simulation of necessary high-resolution microstructural information at all points of a computational domain from continuous low resolution images of the entire domain and few sample high resolution images; (b) quantitative characterization of the microstructure to create effective metrics that can relate microstructural features to critical material behavior of the heterogeneous materials; (c) domain partitioning based on functions of microstructural descriptors. The MDP process delineates regions corresponding to different length scales.

2.1. Microstructure Reconstruction

A prerequisite for creating the morphology-based domain partitioning of the computational domain as a pre-processor for multiscale modeling is information of high-resolution microstructure at all points of the domain. Since it is almost impossible to experimentally obtain contiguous high resolution microscopic images at all points, it is desirable to simulate the local microstructure from micrographs extracted at a few selected locations in the domain. A typical low resolution image of a cast aluminum alloy A319 is shown in Figure 1. The low resolution micrograph does not provide adequate information required for microstructural characterization and modeling. The microstructure reconstruction process generates corresponding high resolution images with clear delineation of the multi-phase morphology.

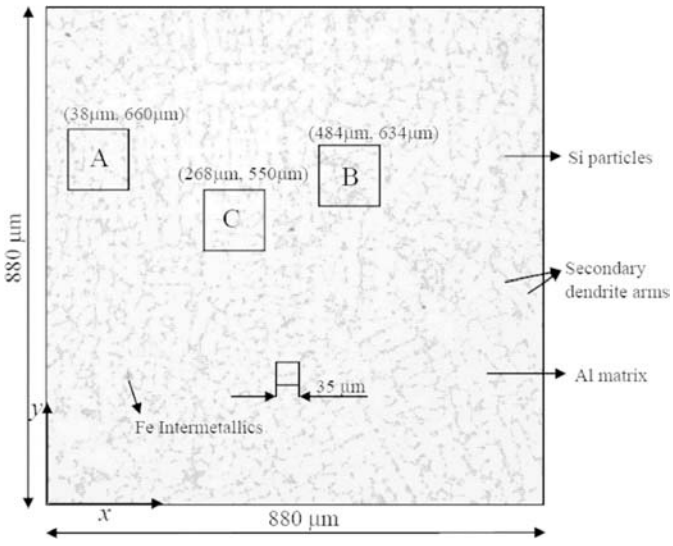

FIG. 1. Low magnification, low resolution digital image of cast aluminum alloy A319, for which high resolution micrograph of a window C is desirable with available high resolution micrographs at other locations A and B.

The digital micrograph of Figure 1 can be resolved into a grid of pixels, with each pixel belonging to a certain level in the grayscale (white-black) hierarchy. For a region Ω_{mic} in the micrograph, the grayscale level of each pixel at (x, y) is represented by an integer valued indicator function $I^g(x,y)$, which can assume any integer value between 0 and 255 at each point of the micrograph. A magnified image of a small region of this micrograph is shown in Figure 2(a). In this paper, magnification refers to the pixel size and hence a magnified image will have larger size of pixels with the same number of grayscale pixels as the original image. Resolution, on the other hand, corresponds to the number of pixels or pixel density in an image. The high resolution microstructure reconstruction incorporates a wavelet based interpolation of low resolution images followed by a gradient based enhancement method (WIGE).

2.1.1. Wavelet Based Interpolation in WIGE Technique

In the WIGE image reconstruction technique, the integer indicator function $I^g(x,y)$ is first interpolated in real space using a basis of wavelet functions. Let a window Ω_w^{lrsm} of the low resolution image encompass a p × q pixel grid. For a higher resolution image Ω_w^{hrsm}, the same window may contain a $p' \times q'$ pixel grid, where $p' > p$ and $q' > q$. The grayscale level of each pixel in the p × q pixel grid corresponds to the value of the indicator function $I^g(x,y)$ at its centroid, which is thus represented by known discrete values at a set of equi-spaced points in the low resolution image window. This is shown in Figure 2(b). Wavelet based interpolation is used for estimating the indicator functions $I^g_{wvlt}(x,y)$ in the high resolution pixel grid. Gaussian functions with continuous derivatives are popular wavelets bases [37, 38] and can effectively represent sharp variations in image features. In encoding a p × q pixel sub-region of a low resolution image, the indicator function may be expressed in terms of a level (m,k) Gaussian wavelet function as

$$I^{g'}_{wvlt}(x,y) = \sum_{1\le n\le p}\sum_{1\le l\le q} \Phi_{m,n,k,l} = \sum_{1\le n\le p}\sum_{1\le l\le q} e^{\frac{-1}{2}(\frac{x-b_n}{a_m})^2} e^{\frac{-1}{2}(\frac{y-d_l}{c_k})^2} \beta_{m,n,k,l} \quad (1)$$

Here (m,k) refer to the wavelet level in a multi-resolution wavelet representation and (n,l) correspond to the discrete translation of the bases in x and y directions, respectively. The parameters b_n, d_l correspond to translation, while a_m, c_k are dilation parameters. This yields a continuous interpolated image representation in terms of indicator function values of the low resolution image. The bases are constructed by translation from one pixel to the next in the p × q pixel sub-region and the region is encoded with p × q Gaussian functions. The wavelet coefficients $\beta_{m,n,k,l}$ can be obtained by solving the matrix equation $\{I^g\} = [F]\{B\}$ where $\{\boldsymbol{I}^g\}$, **[F]** and $\{\mathbf{B}\}$ are matrices of order pq × 1, pq × pq and pq × 1, respectively. The matrix $\{\boldsymbol{I}^g\}$ contains the values of the indicator functions from the available p × q pixel data.

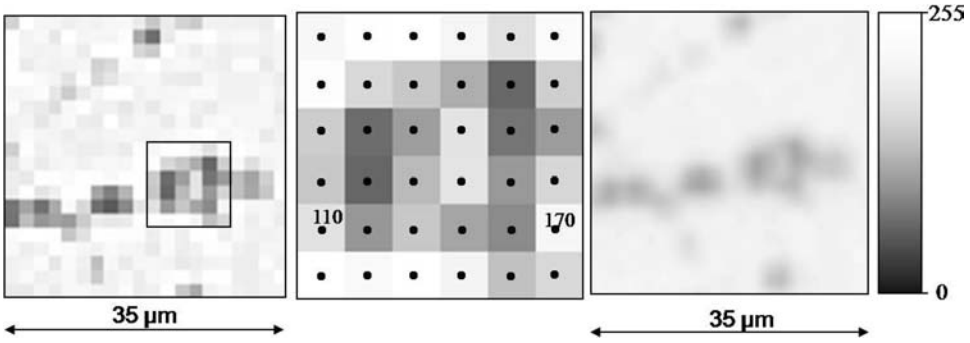

FIG. 2. High magnification 35μm × 35μm images of a region near C, shown in Figure 1: (a) zoomed-in image showing larger pixels but with original resolution; (b) pixels of the square region marked in (a); (c) a higher resolution micrograph of (a) obtained by interpolation.

The matrix **[F]** contains the terms of Gaussian wavelet function, while the matrix {**B**} contains the unknown wavelet coefficients. Numerical studies conducted have indicated that the values for which the system is stable are around p = 6,q = 6.

The interpolation method is tested on the low resolution window marked A, in the A319 micrograph of Figure 1. A high resolution SEM micrograph at the same location is shown in Figure 3(a). The wavelet interpolated image on the 480 × 480 pixel grid is depicted in Figure 3(b). A pixel by pixel subtraction of I^{g}_{wvlt}(x, y) for image 3(b) from image 3(a) is depicted in Figure 3(c). It is clear that interpolation alone is not sufficient for accurate high resolution microstructure, and subsequent image enhancement is essential.

2.1.2. *Gradient Based Post-Interpolation Enhancement*

The enhancement method is developed to augment the wavelet interpolated micrographs with the aid of pixel data from high resolution calibrating images at a few different locations in the domain. The difference indicator function obtained above is expressed as

$$I^{g'}_{diff}(x, y) = I^{g'}_{hrsm}(x, y) - I^{g'}_{wvlt}(x, y) \tag{2}$$

The augmentation methodology requires the creation of a correlation function between $I^{g'}_{diff}(x, y)$ and $I^{g'}_{wvlt}(x, y)$ that will predict the high resolution image in Ω^{hrsm}_{w} from specific features of the interpolated image in Ω^{intm}_{w}. For the interpolated image, the pixel-wise gray-scale level or indicator function and its gradients are considered to be characteristic variables that adequately define the local phase distribution. A discrete correlation function is created between these characteristic variables of the interpolated image Ω^{intm}_{w} and the indicator function value $I^{g'}_{diff}$(x,y) of the difference image Ω^{diff}_{w} at locations where high resolution calibrating micrographs are available. This correlation is expressed in a functional form of the indicator function and its gradients as

$$I^{g'}_{diff}(x, y) = P_{diff}\left(I^{g'}_{wvlt}(x, y), \frac{\partial I^{g'}_{wvlt}}{\partial x_+}, \frac{\partial I^{g'}_{wvlt}}{\partial x_-}, \frac{\partial I^{g'}_{wvlt}}{\partial y_+}, \frac{\partial I^{g'}_{wvlt}}{\partial y_-}\right) \tag{3}$$

Here P_{diff} corresponds to the most probable or expected value of the difference indicator function. The functional form of P_{diff} is not known a-priori. Hence a discrete probability table is constructed from the calibration micrographs Ω^{intm}_{w} and Ω^{diff}_{w} to construct this correlation map. Each bin in the correlation map is represented by a range of values for each of the five variables and contains the values of the difference indicator function $I^{g'}_{diff}$ belonging to the difference image Ω^{diff}_{w}. The range of values

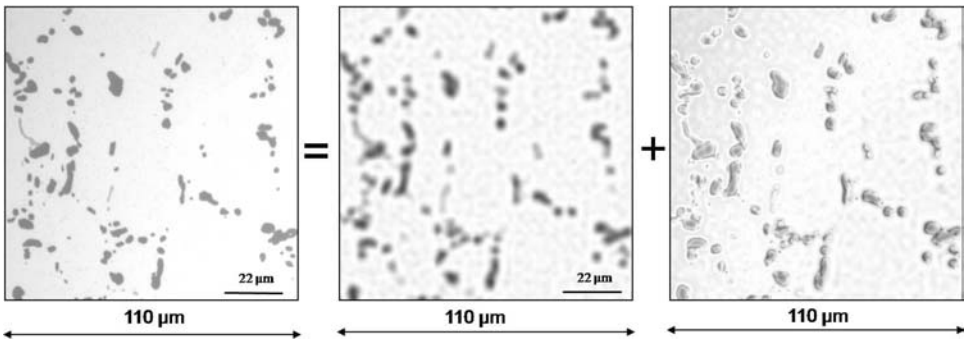

FIG. 3. High resolution micrographs at location A in Figure 1: (a) actual high resolution micrograph; (b) micrograph obtained by wavelet based interpolation in the WIGE algorithm; (c) difference micrograph between (a) and (b).

to be assigned to each bin depends on the nature of variation of the variables. For example, the range $0 \leq I^{g'}_{wvlt} \leq 255$ can be divided into as high as 256 bins or as low as 2 to 3 bins. However, with increasing number of bins, the number of $I^{g'}_{diff}$ entries in each bin will decrease and many of the bins may be empty for the calibration micrographs considered. Sparsity in the correlation bins renders the reliability of this probability table to be low. A moderate number of divisions (∼10–15) is numerically found to be sufficient, as corroborated by convergence studies discussed later. The range of divisions for the gradients is selected in such that they are able to distinguish between regions that belong to the interior and exterior of a given phase.

2.1.3. *Accounting for the Location of the Calibrating Micrographs*

For multi-phase microstructures, the location of high resolution calibrating micrographs in relation to the image being simulated is of considerable importance to the image augmentation process. A major assumption made is that if the calibrating micrographs contain the same constituent phases as the ones being simulated and if they are all produced by the same manufacturing process, the probability functions (P) of local microstructural distributions will have a continuous variation from one micrograph to the next. These probability-wise similar local distributions are necessary for the calibration process to hold. For sharply contrasting micro-regions, calibrating micrographs should be appropriately chosen from regions that represent the essential features of the one being simulated. The effect of the proximity between calibrating and simulated images can be addressed by assigning distance-based weights to the expected values in the probability table. Micrographs closer to the simulated image will have a stronger influence than those that are farther away. This dependence of a microstructure's correlation map on its spatial distance from each of the calibrating micrographs is represented by a "shape function" type interpolation relation, commonly used in finite element analysis, represented for two calibrating micrographs as

$$I^{g'}_{diff}(x, y) = P_{diff}(x, y) = \left(\frac{1-\xi}{2}\right) P_{diff}(x_A, y_A) + \left(\frac{1+\xi}{2}\right) P_{diff}(x_B, y_B) \qquad (4)$$

Here $\xi = (\frac{R_A - R_B}{R_{AB}})$ and R_A and R_B are the distances of a pixel in the simulated image from the corresponding pixels in calibrating micrographs A and B, respectively, and R_{AB} is the distance between them. For microstructures containing a single predominant second-phase in the matrix, e.g. Si for cast aluminum alloys, the different locations, e.g. A and B, may have statistically equivalent expected values of the probability. In this case, the effect of multiple locations in equation 4 will be minimal.

2.1.4. *Validation Test for WIGE Algorithm*

The effectiveness and convergence characteristics of the WIGE algorithm are tested by comparing characteristic metrics of the simulated microstructure with those for a real micrograph at the same location. The n-point statistics developed in [39] are effective metrics for multi-phase microstructure characterization and are used as validation tools. Specifically, the 1-point, 2-point and 3-point statistics are used for this validation. For the low resolution microstructural region of Figure 1, windows at locations A and B are the high resolution calibration micrographs. The WIGE algorithm is used to simulate the image at a window C, for which a high resolution SEM micrograph is available for validation. The 1-point probability function corresponds to the area fraction of the second phase particles. Its variation is plotted in Figure 4(a) as a function of increasing number of divisions in the range of $I^{g'}_{wvlt}$, or bins in the probability table. The value at 0 bins corresponds to the micrograph with no enhancement. The simulated area fraction converges to the SEM image area fraction with about 10 discrete divisions or bins. The

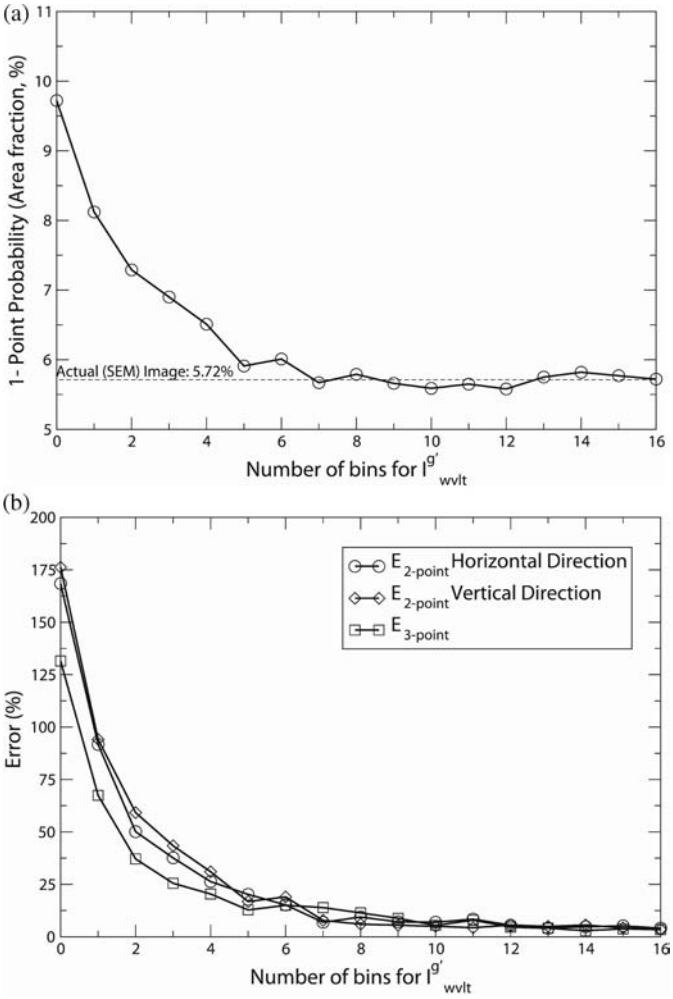

FIG. 4. Convergence plots for n-point statistics: (a) 1-point probability function; (b) error in 2-point and 3-point probability functions.

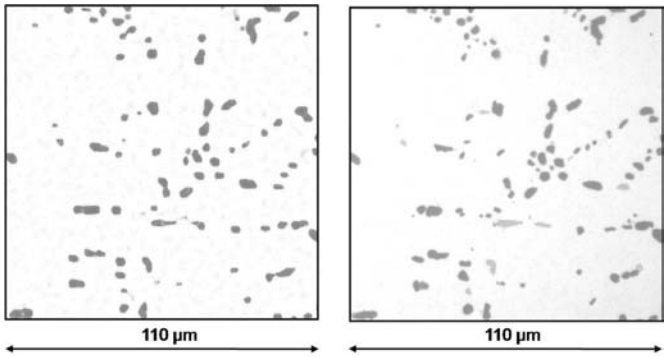

FIG. 5. High resolution micrographs at location C of Figure 1 by the WIGE algorithm: (a) simulated micrograph by using the correlation table; (b) the real high resolution micrograph.

2-point probability function is defined as the probability of finding two points at $r_1(x_1, y_1)$ and $r_2(x_2, y_2)$ (end-points of a line), separated by a distance $r = r_1 - r_2$, in the same phase of the microstructure. The % error in the 2-point probability function between the actual and simulated images is defined as

$$E_{2-\text{point}} = \frac{\sum_{r=0}^{r=L/2} \left| P_{ij}^{SEM} - P_{ij}^{sim} \right|}{\sum_{r=0}^{r=L/2} P_{ij}^{SEM}} * 100\% \tag{5}$$

This error is evaluated along two orthogonal directions and plotted in Figure 4(b). Once again, a fast convergence is noted and the error stabilizes to a near zero value for around 10 bins. Similar convergence behavior is observed for 3-point probability function for three points at the vertices of an isosceles right triangle with interior angles 45°, 45°, and 90°.

It may be concluded that the convergence characteristics of the WIGE algorithm are quite satisfactory with respect to 1-point, 2-point and 3-point correlation functions. Excellent agreement can be seen in the WIGE simulated microstructural image and the corresponding actual micrograph shown in Figures 5(a) and (b). Thus, this method can be applied sequentially to all windows in the computational domain for obtaining high resolution images.

2.2. Microstructure Characterization

Damage in cast aluminum occurs by a combination of particle cracking, microcrack formation and growth in the matrix and coalescence of microcracks. Particle cracking depends on size, aspect ratio and the extent of clustering. Bigger particles or those inside of a cluster show a higher propensity towards cracking. Numerous parameters have been used in the literature to quantify such features [1, 40]. The following parameters are introduced in this work to quantify the size and distribution of particles in microstructure:

(a) Area fraction: A_f is measured as the ratio of total number of pixels belonging to heterogeneity to that of the entire microstructure.

(b) Contour Index: Contour plots of parameters that represent local clustering are very helpful in identifying clusters. Such a contour plot can be generated for a microstructure with N inclusions using the characteristic radius $R_{ch} = \sqrt{\frac{A_{image}}{\pi N}}$ as the field of influence for each heterogeneity. The total area of heterogeneities inside of each characteristic circle is measured as contour intensity (COIN) at a point. The cluster contour index ι is then defined in terms of the contour intensity as

$$\iota = 1 - \frac{Mean(COIN)}{Max(COIN)} \tag{6}$$

The mean and maximum values of COIN are evaluated from all points of the micrograph. A contour index $\iota = 1.0$ denotes a cluster, while values closer to zero indicate uniform distribution. The contour index accounts for the area fraction of particles within a prescribed region. These microstructural parameters are used to perform the MDP process in the following section.

2.3. Multi-Scale Domain Partitioning

An assumption made in the concurrent multi-level models of [16, 17] is that the entire computational domain is initially homogenizable for purely macroscopic computations. However, many heterogeneous materials have multiple length scales from morphological considerations also. Local geometric features render some regions statistically in-homogenizable, i.e. statistical representative volume elements cannot be identified for these regions. Hence, in a true concurrent multi-scale computational model, these regions of geometric non-homogeneity should be identified prior to analysis and concurrently modeled at the microstructural length scales. Once the high resolution microstructural features have been generated for all locations in the computational domain by the WIGE algorithm, the microstructural characterization functions and tools described above can be used for delineating regions with different scales. The objective of this section is to develop criteria that can enable the pre-analysis partitioning of the computational domain into regions of homogeneity and inhomogeneity. For a statistically homogeneous medium, the area fraction is a constant everywhere, i.e. homogeneity can be assumed at regions where A_f does not vary significantly. A homogeneous length scale L_H in the material microstructure is established in [41] from this consideration. L_H is the length scale above which the local variability in area fraction is smaller than a specified tolerance. Below this threshold L_H, it is necessary to change from a homogeneous to a heterogeneous domain representation with explicit delineation of heterogeneities.

The MDP process begins with a coarse discretization of Ω_{comp} into N_p^0 subdomains or partitions, as shown in Figure 6(a). A microstructural unit is defined as a high resolution sub-homogenization length scale microstructural region Ω_{mic} of dimension $\chi^* L_H$ where $\chi < 1$. The factor is chosen as $\chi = 0.5$

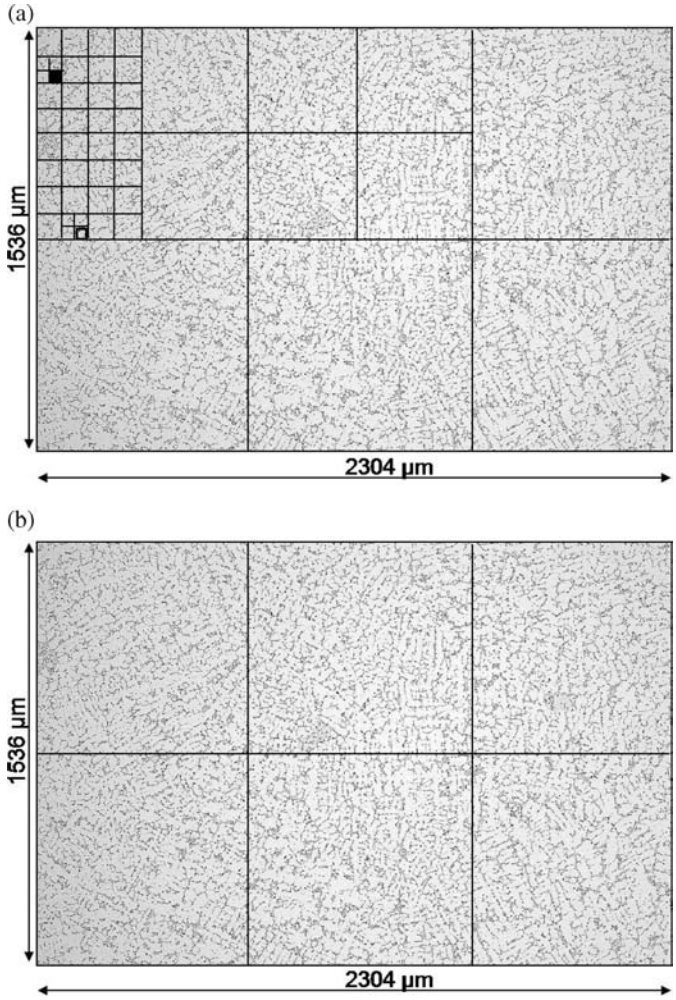

FIG. 6. (a) Microstructural image of cast aluminum alloy A319 to be partitioned; (b) result of the MDP process. Regions in dark boxes are identified as inhomogeneous and need to be analyzed with micromechanical models.

in this work. Any given subdomain i is assumed to be made up of M^i underlying microstructural units. Statistical functions representing the variation of a descriptor in the M^i microstructural units are evaluated for successive partitioning of a subdomain i. The area fraction A_f and contour index ι are used to construct a refinement criteria function. It is constructed in terms of the mean parameters $\mu(A_f)$ and $\mu(\iota)$ for the M^i microstructural units within each subdomain i, and is expressed as $F_i = \mu(A_f)\mu(\iota)$. The refinement function is evaluated in each subdomain, together with those in each of its four divisions $F_i(l)$, $l = 1.4$. A subdomain i is partitioned only if the following criterion is attained for any of the four sub-regions $\frac{F_i - F_i(l)}{F_i} > C_{f1}$. The prescribed tolerance is $C_{f1} = 0.10$ corresponding to 10% variation. The successive partitioning process reduces the subdomain size locally, and may ultimately reach the homogeneous scale limit L_H. Once L_H is reached, only one additional step of further partitioning is possible. The level below L_H is not homogenizable and hence cannot be refined any further. A special criterion is required for this partitioning. Each of the subsequent partitions contains only one microstructural unit M^{loc} of dimension $0.5^* L_H$. It is not possible to evaluate the statistical functions for a single M^{loc}. The criterion is constructed in terms of the variation of average local area fraction A_f. Partitioning below L_H is governed by the criterion $(\frac{(A_f)_i}{(A_f)_\Omega})(\frac{(A_f)_i - (A_f)_i(l)}{(A_f)_i}) > C_{f2}$. In this criterion the first term corresponds to the local area fraction of subdomain i, with respect to the area fraction of the entire domain and the second term corresponds to the comparison of local area fraction to its four divisions. These terms together provide an estimate of heterogeneity of the subdomain i. Any sub-domain below the L_H threshold is characterized by significant variation in the local area fraction. Consequently those partitions for which the variation is really large are classified as nonhomogeneous and opened up for explicit microstructural representation in the multi-level model. The factor C_{f2} is taken as 0.75, corresponding to a 75% difference in the critical regions of the microstructure. The combined microstructure simulation-characterization-partitioning method delineates the hierarchy of scales in the computational model as demonstrated in the following example.

2.4. A Numerical Example

The morphology based domain partitioning (MDP) methodology is applied to the microstructures of cast aluminum alloy A319 with secondary dendrite arm spacing of 23μm. The low resolution computational micrograph Ω_{comp} of dimensions 2304 μm $\times$ 1536 μm is shown in figure 6(a). The WIGE algorithm generates high resolution images of all points in Ω_{comp} by constructing a correlation table, from two 110 μm $\times$ 110 μm high resolution SEM image windows. The locations of these two windows are shown as A and B in Figure 1. The homogenization length scale L_H is evaluated using the methodology in [30] with a tolerance of 0.2 on coefficient of variation of area fraction and is obtained as $L_H = 96$ μm.

The MDP process begins by dividing the computational domain Ω_{comp} into 6 subdomains. This initial partition is shown in Figure 7(a). Successive partitioning progresses according to the refinement criteria in section 2.3, until the subdomain size reaches L_H. After three cycles of successive refinement, the partition size reaches $L_H = 96$ μm. The final partitioned computational domain is shown in Figure 6(b). The size of the inhomogeneous domain is $\sim$48 μm. The inhomogeneous regions identified by the MDP process need to be modeled at the micromechanical level in the concurrent multi-scale analyses and simulations. One of two such regions marked with a dark box in Figure 6(b) is shown in Figure 7(a). Micromechanical analysis of such regions is discussed in the following section.

3. LOCALLY ENRICHED VCFEM FOR DUCTILE FRACTURE OF PARTICLE REINFORCED METALLIC MATERIALS

Shown in Figure 7, the Voronoi cell finite element model (VCFEM) naturally evolves by tessellation of the heterogeneous

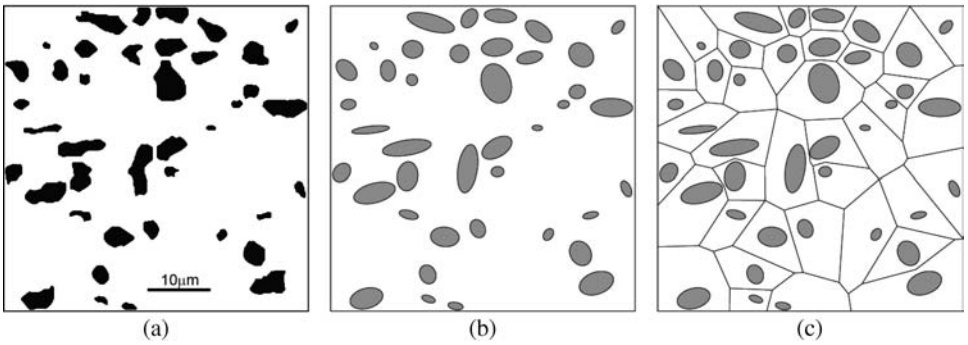

FIG. 7. (a) Micrograph at region marked in Figure 6(b); (b) equivalent microstructure with elliptical particles; (c) Voronoi cell FEM mesh of the equivalent microstructure.

microstructure into a network of multi-sided Voronoi cells. Each Voronoi cell in VCFEM represents the neighborhood of heterogeneities such as particle or inclusions in the microstructure. The particles are represented by ellipses or by multi-sided polygonal domains in this paper. The particles are assumed to be brittle elastic materials while the matrix is assumed to be ductile and represented by a pressure dependent elasto-plastic model for porous materials.

The VCFEM formulation is based on the assumed stress hybrid formulation [11–15], in which equilibrated stress fields are assumed in the interior of each element and compatible displacements are assumed on the boundary of each element and on the particle-matrix interface. After particle fragmentation, the topology of each element changes from two constituent phases to three constituents with the inclusion of the crack, as shown in Figure 8. In the subsequent ductile fracture phase, regions in each Voronoi cell that exhibit softening in the stress-strain behavior is enriched adaptively with finite deformation, displacement based finite elements. The enriched Voronoi cell consists of the matrix phase Ω_m, the particle phase Ω_c and a softening region of ductile damage Ω_s, as shown in Figure 9.

Particle cracking in the microstructure naturally gives rise to stress concentrations or singularities, which in turn cause local matrix failure. With continued deformation beyond particle cracking, material points in the matrix lose their load carrying capacity due to local void growth and strain softening. These regions are identified and adaptively converted to softened regions Ω_s, for which a displacement based finite element mesh is automatically generated. Though in the schematics of Figures 8 and 9 ductile matrix cracking is preceded by particle cracking, the two mechanisms exist simultaneously and independently in the model. Stresses σ_{ij}^s in the softened region are generated by using large deformation kinetics with an implicit backward Euler integration rule [42]. For the superposed displacement elements, a type of h-type of refinement strategy proposed in [43] is used to reduce the mesh sensitivity. The B-bar method suggested in [44] is used for avoiding the volume locking problem for nearly incompressible plasticity. The rotated Cauchy stress rate [45] is used as an objective stress measure for the finite deformation formulation within these narrow localization zones. A summary of the LE-VCFEM formulation is presented here.

3.1. VCFEM Formulation with Particle Cracking

For particle cracking in an elastic-plastic matrix, an incremental element energy functional Π_e^{PC} is defined for each Voronoi cell element in terms of stress increments in the matrix and particle phases $\Omega_m \cup \Omega_c$, and displacement increments on the element boundary $\partial\Omega_e$, particle-matrix interface $\partial\Omega_c$ as well as on the crack boundary $\partial\Omega_{cr}$. The first variation of Π_e^{PC}

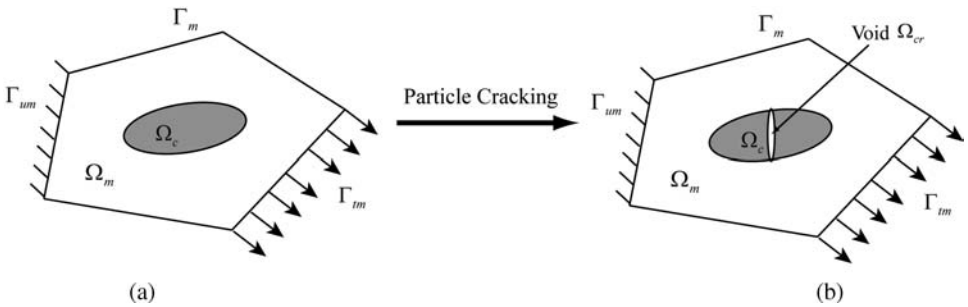

FIG. 8. Evolution of a Voronoi cell element (a) without damage and (b) with particle cracking.

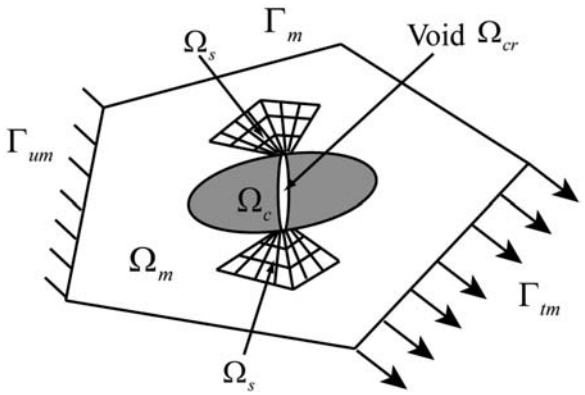

FIG. 9. Locally enriched VCFEM with superposed displacement elements in the softening region Ω_s.

is expressed as

$$\begin{aligned}\delta\Pi_e^{PC}(\Delta\sigma_{ij},\Delta\bar{u}_i) &= -\int_{\Omega_m\cup\Omega_c}\Delta\varepsilon_{ij}\delta\Delta\sigma_{ij}d\Omega\\ &-\int_{\Omega_m\cup\Omega_c}\varepsilon_{ij}\delta\Delta\sigma_{ij}d\Omega+\int_{\partial\Omega_e}\delta\Delta\sigma_{ij}n_j^e\Delta\bar{u}_i d\partial\Omega\\ &+\int_{\partial\Omega_e}(\sigma_{ij}+\Delta\sigma_{ij})n_j^e\delta\Delta\bar{u}_i d\partial\Omega-\int_{\Gamma_{tm}}(\bar{t}_i+\Delta\bar{t}_i)\delta\Delta u_i d\Gamma\\ &-\int_{\partial\Omega_c}\left(\delta\Delta\sigma_{ij}^m-\delta\Delta\sigma_{ij}^c\right)n_j^c\Delta\bar{u}_i' d\partial\Omega\\ &-\int_{\partial\Omega_c}\left(\sigma_{ij}^m+\Delta\sigma_{ij}^m-\sigma_{ij}^c-\Delta\sigma_{ij}^c\right)n_j^c\delta\Delta\bar{u}_i' d\partial\Omega\\ &-\int_{\partial\Omega_{cr}}\delta\Delta\sigma_{ij}^c n_j^{cr}\Delta\bar{u}_i'' d\partial\Omega-\int_{\partial\Omega_{cr}}\left(\sigma_{ij}^c+\Delta\sigma_{ij}^c\right)n_j^{cr}\delta\Delta\bar{u}_i'' d\partial\Omega\end{aligned}\tag{7}$$

Here $\bar{\mathbf{t}}$ is the external traction on the traction boundary Γ_{tm} and $\mathbf{n}$ is the outward normal on respective boundary segments. The corresponding total energy functional for the entire computational domain is expressed as $\sum_{e=1}^{NEL}\Pi_e^{PC}$. From the stationarity conditions of the functional, the following Euler's equations are:

$$\begin{aligned}\nabla\Delta\mathbf{u}&=\Delta\boldsymbol{\varepsilon}\quad\text{in}\quad\Omega_e;\\ (\boldsymbol{\sigma}+\Delta\boldsymbol{\sigma})\cdot\mathbf{n}^{e+}&=-(\boldsymbol{\sigma}+\Delta\boldsymbol{\sigma})\cdot\mathbf{n}^{e-}\quad\text{on}\quad\partial\Omega_e;\\ (\boldsymbol{\sigma}+\Delta\boldsymbol{\sigma})\cdot\mathbf{n}^{e+}&=\bar{\mathbf{t}}+\Delta\bar{\mathbf{t}}\quad\text{on}\quad\Gamma_{tm}\\ (\boldsymbol{\sigma}^c+\Delta\boldsymbol{\sigma}^c)\cdot\mathbf{n}^c&=(\boldsymbol{\sigma}^m+\Delta\boldsymbol{\sigma}^m)\cdot\mathbf{n}^c\quad\text{on}\quad\partial\Omega_c;\\ (\boldsymbol{\sigma}^c+\Delta\boldsymbol{\sigma}^c)\cdot\mathbf{n}^{cr}&=\mathbf{0}\quad\text{on}\quad\partial\Omega_{cr}\end{aligned}\tag{8}$$

Superscript + and − denote elements on both sides of the boundary $\partial\Omega_e$. $\bar{\mathbf{t}}$ is the external traction on the traction boundary Γ_{tm}. The equilibrated stress field $\Delta\sigma_{ij}$ is interpolated independently in the matrix and particle phases of the Voronoi cell. Conveniently, the Airy's stress function $\Phi(x, y)$ may be used to derive the equilibrated stress increments in the VCFEM formulation for rate independent elasto-plasticity [13, 14]. Compatible displacement fields $\Delta\bar{u}_i$ are independently interpolated on the element/particle/crack boundaries using standard shape functions. A-priori assumptions on equilibrated stress increments $\Delta\boldsymbol{\sigma}$ and constitutive relationships along with Euler equations, completely define the boundary value problem for a heterogeneous domain undergoing particle cracking.

The VCFEM has been successfully applied for the simulation of particle cracking in reinforced metal matrix composites [12–14]. Complete particle cracking is assumed to occur at the onset of damage, thereby avoiding crack propagation within each particle. A high aspect ratio ellipse ($a/b = 10$) is used to represent a particle crack. The particle crack initiation criterion is expressed in the form of a Weibull probability function that depends on the local principal stresses and the volume of the particles in the composite [12]. For the i-th particle, the probability of fracture P_i is expressed as

$$P_i\left(v,\sigma_i^I\right)=1-\exp\left[-\frac{v}{v_0}\left(\frac{\sigma_i^I}{\sigma_w}\right)^m\right]\tag{9}$$

where m and σ_w are the Weibull modulus and the characteristic strength, respectively. v is the volume of the i-th particle. v_0 is a reference volume, which is taken as the average volume of all particles and σ_i^I is the maximum principal stress in the i-th particle.

3.2. Particle and Matrix Cracking Causing Ductile Fracture

Ductile failure occurs by the combined phenomena of crack nucleation, micro-void growth and eventual void coalescence. Voids nucleate with particle fragmentation, subsequently grow in the matrix with large plastic deformation, and finally coalesce with each other to advance the local fracture zone. A nonlocal form of the Gurson-Tvergaard-Needleman (GTN) model proposed in [46, 47] is used to model the post-nucleation ductile fracture in the matrix material. In this model, a pressure yield surface Φ is written in terms of the evolving void volume fraction f^* as

$$\Phi=\left(\frac{q}{\sigma_0}\right)^2+2f^*q_1\cosh\left(-\frac{3q_2p}{2\sigma_0}\right)-(1+q_3f^{*2})\tag{10}$$

where q and p are, respectively, the equivalent Von-Mises stress and hydrostatic pressure in the matrix, and q_1, q_2, q_3 are constants calibrated from numerical analyses of a periodic array of voids. $\sigma_0(\varepsilon^p)$ is the strength of the matrix material in the absence of voids. To avoid inherent mesh sensitivity of numerical failure predictions, a non-local evolution equation for the void volume fraction is implemented. The nonlocal void volume fraction growth rate at a material point $\mathbf{x}$ is written as:

$$\begin{aligned}\dot{f}_{nl}&=\frac{1}{W(\mathbf{x})}\int_{\Omega_m}\dot{f}(\bar{\mathbf{x}})w(|\mathbf{x}-\bar{\mathbf{x}}|)d\Omega;\\ W(\mathbf{x})&=\int_{\Omega_m}w(|\mathbf{x}-\bar{\mathbf{x}}|)d\Omega\\ w(z)&=\left[\frac{1}{1+(z/L)^p}\right]^q,\quad p=8,q=2\end{aligned}\tag{11}$$

The weighting function $w(z)$ has a value close to 1 within a characteristic length scale radius L ($z \leq L$) and diminishes rapidly outside the material radius. The explicit introduction of the length scale parameter L regularizes the localization problem and prevents the matrix crack from being unreasonably small. In VCFEM, the FE mesh is generated based on tessellation of the real microstructure and hence the mesh has a inherent connection to the material microstructure. The length scale parameter L is chosen based on the maximum size of the Voronoi cell finite elements. The local void growth rate is governed by the relation:

$$\dot{f} = (1 - f_{nl})\, \dot{e}^p_{kk} + A(\bar{\varepsilon}^p)\dot{\bar{\varepsilon}}^p \tag{12}$$

where the evolution of effective plastic strain is written as:

$$\sigma_0 \dot{\bar{\varepsilon}}^p = \sigma_{ij} \dot{\lambda} \frac{\partial \Phi}{\partial \sigma_{ij}} \tag{13}$$

The second term in equation (12) is for void nucleation controlled by plastic strain as suggested in [46], where

$$A = \frac{f_N}{s_N \sqrt{2\pi}} \exp\left[-\frac{1}{2} \left(\frac{\bar{\varepsilon}^p - \varepsilon_N}{s_N} \right)^2 \right] \tag{14}$$

For void coalescence, an acceleration function proposed in [47] is used,

$$f^* = \begin{cases} f_{nl} & f_{nl} \leq f_c \\ f_c + \dfrac{f_u^* - f_c}{f_f - f_c} (f_{nl} - f_c) & f_{nl} > f_c \end{cases} \tag{15}$$

Here f_c is the critical void volume fraction at which void coalescence first occurs and f_f is the value at final failure, which means the material loses all load capacity as $f_{nl} \rightarrow f_f$ ($f^* \rightarrow f_u^* = 1/q_1$). To avoid the numerical difficulties, ($f_{nl} \rightarrow 0.95 f_f$) is used instead of ($f_{nl} \rightarrow f_f$).

A problem with the stress based VCFEM is that non-uniqueness in the displacement solutions in the softening phase of material deformation will result in numerical instabilities. To avert this shortcoming, the softening region Ω_s within each Voronoi cell element is adaptively augmented with displacement based finite elements as shown in Figure 9. Finite deformation, pressure dependent elasto-plasticity formulation is used for the of displacement finite elements in the local softening region.

Once the displacement based local FE region Ω^s is overlaid, a parameter mapping process maps local stresses, strains and material internal variables from the VCFEM domain to displacement elements. A superscript s corresponds to variables associated with the enriched softening regions Ω^s. The formulation guarantees that the displacement $\mathbf{u}^s$ on the boundary $\partial\Omega_s$ is compatible with the displacement $\bar{\mathbf{u}}$, $\bar{\mathbf{u}}'$ and $\bar{\mathbf{u}}''$, respectively, on the $\partial\Omega_m$, $\partial\Omega_c$ and $\partial\Omega_{cr}$, i.e.

$$\begin{aligned} &\mathbf{u}^s = \bar{\mathbf{u}} \quad \text{on} \quad \partial\Omega_s \cap \partial\Omega_m; \mathbf{u}^s = \bar{\mathbf{u}}' \quad \text{on} \quad \partial\Omega_s \cap \partial\Omega_c; \\ &\mathbf{u}^s = \bar{\mathbf{u}}'' \quad \text{on} \quad \partial\Omega_s \cap \partial\Omega_{cr} \end{aligned} \tag{16}$$

With the addition of the enriched softening region Ω_s, the VCFEM formulation is modified with the augmentation of the energy functional of equation (7). The corresponding incremental potential energy ΔA for the displacement elements is added with appropriate boundary conditions are added to incremental element energy functional Π_e^{PC} to yield an enriched energy functional Π_e^{EN} with an added independent variable $\Delta\mathbf{u}^s$. The corresponding first variation of Π_e^{EN} is written as

$$\begin{aligned} \delta\Pi_e^{EN}(\Delta\sigma_{ij}, \Delta\bar{u}_i, \Delta u_i^s) = \delta\Pi_e^{PC} - \int_{\Omega_s} (\sigma_{ij}^s + \Delta\sigma_{ij}^s)\delta\Delta\varepsilon_{ij}^s d\Omega \\ + \int_{\partial\Omega_s} \delta\Delta\sigma_{ij} n_j^s \Delta u_i^s d\partial\Omega + \int_{\partial\Omega_s} (\sigma_{ij} + \Delta\sigma_{ij}) n_j^s \delta\Delta u_i^s d\partial\Omega \end{aligned} \tag{17}$$

where Δu_i^s is the displacement increment for the displacement elements. The displacement interpolation in terms of the nodal displacements are expressed as

$$\{\Delta\mathbf{u}^s\} = \{\mathbf{N}^s\}\{\Delta\mathbf{q}^s\} \tag{18}$$

Additional Euler equations resulting from equation (16) are:

$$\begin{aligned} (\boldsymbol{\sigma} + \Delta\boldsymbol{\sigma}) \cdot \mathbf{n}^s &= (\boldsymbol{\sigma}^s + \Delta\boldsymbol{\sigma}^s) \cdot \mathbf{n}^s \quad \text{on} \quad \partial\Omega_s; \\ \Delta\mathbf{u}^s &= \Delta\bar{\mathbf{u}} \quad \text{on} \quad \partial\Omega_s \cap \partial\Omega_m \\ \Delta\mathbf{u}^s &= \Delta\bar{\mathbf{u}}' \quad \text{on} \quad \partial\Omega_s \cap \partial\Omega_c; \\ \Delta\mathbf{u}^s &= \Delta\bar{\mathbf{u}}'' \quad \text{on} \quad \partial\Omega_s \cap \partial\Omega_{cr} \end{aligned} \tag{19}$$

The first Euler equation ensures the traction reciprocity on the softening region interface $\partial\Omega_s$. The next three equations ensure the displacement increment continuity on $\partial\Omega_s \cap \partial\Omega_m$, $\partial\Omega_s \cap \partial\Omega_c$ and $\partial\Omega_s \cap \partial\Omega_{cr}$.

3.2.1. Integration Algorithms in the LE-VCFEM Formulation

The adapted LE-VCFEM couples a small deformation hybrid stress-based region Ω_m and a finite deformation displacement-based softening region Ω_s. This necessitates different integration algorithms for elements in different regions. In the hybrid stress-based region a strain update algorithm implementing the *Regula Falsi* scheme is used to calculate plastic strains, stresses and state variables for a given stress increments $\Delta\boldsymbol{\sigma}$ [13, 14]. For the displacement elements, a backward Euler method proposed in [42] is used for stress and plastic strain update in an updated Lagrangian formulation introduced in [45]. An objective rate of the rotated Cauchy stress $\boldsymbol{\sigma}_{\mathbf{R}}^{\mathbf{s}} = \mathbf{R}^{\mathbf{T}}\boldsymbol{\sigma}^{\mathbf{s}}\mathbf{R}$, in which $\mathbf{R}$ is a proper orthogonal tensor representing pure rotation obtained from the polar decomposition of $\mathbf{F}$, i.e. $\mathbf{R} = F\mathbf{U}^{-1}$ decomposition. The subscript "R" corresponds to variables in a rotated configuration. The rotated Cauchy stress is updated to the $n+1$-th increment using the equation

$$\left(\boldsymbol{\sigma}_{\mathbf{R}}^{\mathbf{s}}\right)^{n+1} = \left(\boldsymbol{\sigma}_{\mathbf{R}}^{\mathbf{s}}\right)^{n} + \Delta\boldsymbol{\sigma}_{\mathbf{R}}^{\mathbf{s}}; \quad \text{where} \quad \Delta\boldsymbol{\sigma}_{\mathbf{R}}^{\mathbf{s}} = (\mathbf{C}^{e-p})^{n+1} : \Delta\boldsymbol{\varepsilon}_{\mathbf{R}}^{\mathbf{s}} \tag{20}$$

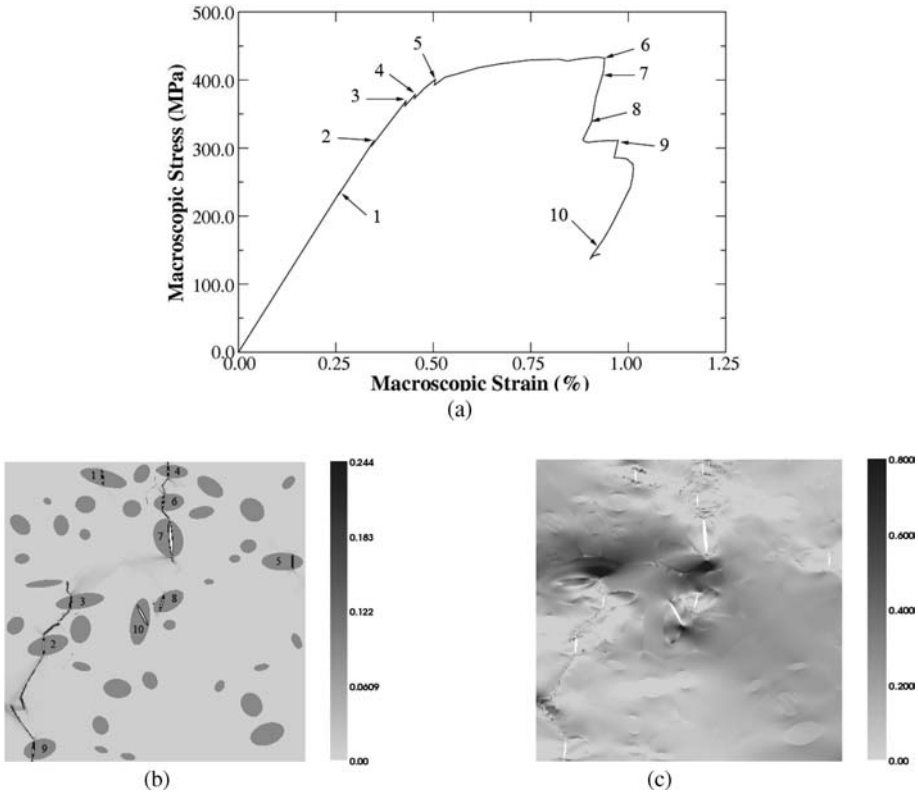

FIG. 10. (a) Macroscopic stress-strain response; contour plot of (b) the void volume fraction and (c) the stress σ_{xx} (GPa) at $\bar{\varepsilon}_{xx} = 1.57\%$. The numbers in figures (a,b) indicate the sequence of particle cracking.

and $\mathbf{C}^{e-p}$ is the elasto-plastic tangent stiffness in the rotated configuration:

$$C^{e-p}_{ijkl} = \left(\frac{\partial(\boldsymbol{\sigma}^{\mathbf{s}}_{\mathbf{R}})_{ij}}{\partial(\boldsymbol{\varepsilon}^{\mathbf{s}}_{\mathbf{R}})_{kl}} \right) \tag{21}$$

An iterative solution procedure is used in the backward Euler integration method.

3.2.2. Mapping State Variable from Assumed Stress to Assumed Displacement Regions in VCFEM

Once displacement elements are identified and superposed in the softening regions in LE-VCFEM, it is important to map all the parameters, e.g. stress, strain, and other internal variables, from the assumed stress model with stress interpolations to the assumed displacement elements. The super-convergent patch recovery or SPR method developed in [48] is used to map values from the VCFE mesh to 9-noded bi-quadratic displacement elements based on Lagrange polynomials. In this process, a complete 4th order polynomial expansion is used for all parameters as:

$$v^*_p = \mathbf{Pa}, \quad \mathbf{P} = [1, x, y, x^2, xy, y^2, x^3, x^2y, xy^2, y^3, x^4, x^3y, x^2y^2, xy^3, y^4] \tag{22}$$

where v^*_p represents components of stress, strain, equivalent plastic strain $\bar{\varepsilon}^p$ and void volume fraction f at nodal points of the 9-noded displacement elements and **a** is a set of unknown parameters. The corresponding parameters at integration points are interpolated from nodal values using shape functions for QUAD-9 elements as:

$$v = \mathbf{N}\mathbf{v}^*_p \tag{23}$$

3.3. A Numerical Example of Ductile Failure in Cast Aluminum Microstructure

Figure 7(a) shows the micrograph of a reinforced Al-SiC composite consisting of 40 SiC particles. Figure 7(c) shows the corresponding Voronoi cell mesh for an equivalent simulated microstructure. The Al matrix is assumed to be ductile and is modeled by elastic-plasticity constitutive relations for porous materials with the following properties: Young's modulus $E = 66\,\text{GPa}$, Poisson's ratio $\upsilon = 0.33$, initial void volume fraction $f_0 = 0.004$. The post yield behavior for the pure matrix material without voids is expressed by the Ramberg-Osgood law ($\sigma_m = \sigma_0(\frac{\varepsilon^p_m}{\alpha\varepsilon_0})^{\frac{1}{n}}$), where the initial flow stress of the matrix $\sigma_0 = 440\,\text{MPa}$, ε_0 is the strain at yield ($\varepsilon_0 = \sigma_0/E$), $\alpha = 3/7$ and the strain hardening exponent $n = 12.5$. The reinforcing SiC particles are assumed to be brittle and are modeled with the linear elastic properties: Young's modulus $E = 400\,\text{GPa}$, Poisson's

ratio $v = 0.2$. For particle cracking, ($m = 2.4$, $\sigma_w = 1.32$ GPa) are used in equation (9) for Weibull model. For the GTN model, ($q_1 = 1.5$, $q_2 = 1.0$, $q_3 = q_1^2 = 2.25$) are used in equation (10) and $L = 0.05 \times$ (maximum size of the Voronoi cell elements) $= 1\ \mu$m is used in equation (11) for nonlocal model. And ($\varepsilon_N = 0.1$, $s_N = 0.1$, $f_N = 0.1$) are used in equation (14) for nucleation. The microstructure is subjected to a macroscopic tension strain $\bar{\varepsilon}_{xx} = 1.57\%$, applied on the left side of the computational domain. The results of the simulation are shown in Figure 4. Figure 10(a) shows the macroscopic strain-stress response, with the explicit effect of particle cracking followed by ductile matrix fracture. The cracked particle numbers are shown in Figure 10(b). The first 9 particles crack in isolation and do not affect the cracking of others. During this period, no softening in the stress-strain behavior is observed. Softening, manifested by a drop in the stress-strain curve corresponding to a negative stiffness, starts after the tenth particle has cracked followed by significant plastic deformation and void growth in the matrix. From Figure 10(b), it is evident that the subsequent sequence of particle and matrix cracking occur in a very narrow band of the microstructure and hence a dominant crack path is observed. The sequence of particle cracking is shown in the stress-strain plot of Figure 10(a). The figure shows that particles (# 6, 7, 8, 9, and 10) crack after the dominant ductile crack has developed in the microstructure. Contour plots of the void volume fraction in the matrix (with $f_c = 0.15$, $f_f = 0.25$) and the stress in the loading direction for $\bar{\varepsilon}_{xx} = 1.57\%$ are shown in Figures 10(b,c). Near the dominant fracture path, the stress σ_{xx} decreases to near zero.

4. CONTINUUM DAMAGE MECHANICS MODEL FOR DUCTILE MATERIALS BY HOMOGENIZATION OF MICROMECHANICAL RESPONSE FUNCTIONS

In this section, a macroscopic continuum damage mechanics model is developed for multi-phase ductile materials containing non-uniform dispersion of brittle particles. The damage model, developed for plane strain analysis, can be used in macroscopic analysis models for predicting ductile failure in the material. The anisotropic damage model is chosen to follow the general framework of the Gurson-Tvergaard-Needleman (GTN) model [46, 47]. To accommodate non-proportional loading, the anisotropic constitutive and damage models are expressed in the principal material and principal damage coordinate systems respectively. A pre-matrix cracking homogenization based continuum damage model for ductile composites undergoing particle cracking only, has been developed by Ghosh et al. in [16].

4.1. Homogenized Anisotropic Constitutive Model Based on the GTN Model

The GTN model based homogenized anisotropic elastic-plastic constitutive model for materials undergoing microstructural ductile fracture considers only void growth for plane strain problems. The anisotropic yield criterion for porous ductile materials containing a dispersion of particles depends on hydrostatic stress measures and void volume fraction, and may be written as

$$\phi = \frac{\Sigma_{eq}^2}{Y_f^2(W_p)} + 2Q_1 f \cosh\left(\frac{Q_a\Sigma_{xx} + Q_b\Sigma_{yy} + Q_c\Sigma_{zz}}{Y_f(W_p)}\right) - 1 - (Q_1 f)^2 = 0 \tag{24}$$

where Σ_{ij} is the macroscopic homogenized stress in a composite medium W_p is the plastic work and Y_f is the flow stress in shear. As stated in equation (12), the evolution of f is governed by the plastic strain and its rate, as well as f itself. The increment of macroscopic plastic strain is obtained from the yield criterion by using an associated flow rule for hardening materials, i.e. $\dot{e}_{ij}^p = \dot{\lambda}\frac{\partial\phi}{\partial\Sigma_{ij}}$. For plane strain, the equivalent stress Σ_{eq} in the matrix material without voids (microstructure consisting of matrix and particles) is represented using Hill's [49] anisotropic yield function as

$$\Sigma_{eq}^2 = F(W_p)(\Sigma_{yy} - \Sigma_{zz})^2 + G(W_p)(\Sigma_{zz} - \Sigma_{xx})^2 + H(W_p)(\Sigma_{xx} - \Sigma_{yy})^2 + C(W_p)\Sigma_{xy}^2 \tag{25}$$

The anisotropy parameters $F(W_p)$, $G(W_p), H(W_p)$ and $C(W_p)$ are functions of the plastic work W_p that are calibrated from homogenization studies with material without voids. Likewise, the parameters $Q_1(W_p)$, $Q_a(W_p)$, $Q_b(W_p)$ and $Q_c(W_p)$ corresponding to an effective hydrostatic stress are calibrated from homogenization studies on materials containing voids. The asymptotic expansion based homogenization of microscopic variables in the microstructural RVEs using periodicity assumptions on the boundary has been discussed in [16, 17, 50]. Homogenization studies in this work are conducted with the micromechanical LE-VCFEM analysis discussed in section 3. The calibrated parameters will depend on the microstructural characteristics of the RVE's, and their calibration process for each RVE is discussed in section 4.2. When $f = 0$, equation (23) reduces to the yield criterion for an anisotropic composite material without porosity, and hence

$$\phi = \frac{F(W_p)(\Sigma_{yy} - \Sigma_{zz})^2 + G(W_p)(\Sigma_{zz} - \Sigma_{xx})^2 + H(W_p)(\Sigma_{xx} - \Sigma_{yy})^2 + C(W_p)\Sigma_{xy}^2}{Y_f^2(W_p)} - 1 = 0 \tag{26}$$

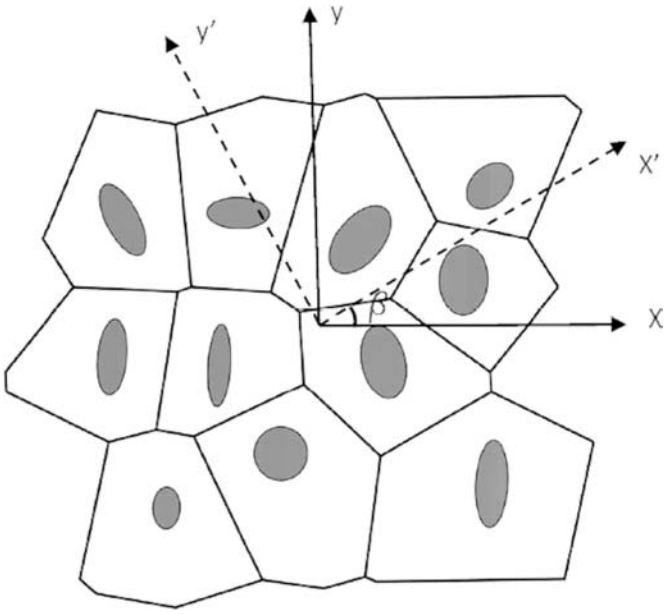

FIG. 11. RVE with randomly distributed particles showing principal axes of material anisotropy.

This yield criterion is defined in the principal axes of material symmetry. The material is assumed to be orthotropic with respect to the principal coordinate system. Material anisotropy is determined not only by the morphology of microstructures, such as size, shape and distribution of particles, but also the evolution of plastic deformation and damage in the microstructure during the loading process. It is assumed that at every load step, material remains orthotropic with respect to the evolving material axis. At every load step, the angle β in Figure 11 corresponding to principal axes of anisotropy for plane strain conditions is determined from the conditions required to keep the tangent modulus $E^{\tan}_{ijkl}$ orthotropic. Consequently, terms coupling the normal and shear components in the transformed tangent modulus are set to zero, i.e. $(E^{\tan}_{1112})' = (E^{\tan}_{2212})' = (E^{\tan}_{3312})' = 0$, where

$$\left(E^{\tan}_{ijkl}\right)' = Q_{im}Q_{jn}Q_{kp}Q_{lq}E^{\tan}_{mnpq} \quad \text{where}$$
$$[\mathbf{Q}] = \begin{bmatrix} \cos\beta & \sin\beta & 0 \\ -\sin\beta & \cos\beta & 0 \\ 0 & 0 & 1 \end{bmatrix} \tag{27}$$

4.2. Evaluation of Constitutive Parameters Variables in the Homogenized Constitutive Model

4.2.1. $Y_f(W_p)$ and C in Equation (26)

As defined in equation (24), $Y_f(W_p)$ is taken as the flow stress in shear. A microscopic boundary value problem of the RVE is solved for incremented pure shear loading ($e_{xx} = e_{yy} = 0,\ e_{xy} \neq 0$), which is followed by homogenization. This is done by applying pure macroscopic shear strain on the RVE with periodic boundary conditions, as detailed in [16]. The macroscopic plastic work, stresses and strains are evaluated by averaging the microstructural variables using following equations:

$$\dot{W}_p = \frac{1}{\Omega}\int_\Omega \sigma_{ij}\dot{\varepsilon}^p_{ij}\,d\Omega, \quad \Sigma_{ij} = \frac{1}{\Omega}\int_\Omega \sigma_{ij}d\Omega, \quad e_{ij} = \frac{1}{\Omega}\int_\Omega \varepsilon_{ij}d\Omega \tag{28}$$

For pure shear loading condition, $\Sigma_{xx} = \Sigma_{yy} = \Sigma_{zz} = 0$ and $\Sigma_{xy} \neq 0$. The parameter C in equation (25) is first set to 3, then $Y_f(W_p) = \sqrt{3}\Sigma_{xy}$. Finally, the flow stress is plotted as a function of plastic work W_p, as shown in Figure 12(a).

4.2.2. Parameters F, G and H

(i) A set of numerical experiments for given RVE (without voids and without particle fragmentation) with different loading conditions are performed using LE-VCFEM and homogenization theory. The different loading conditions are

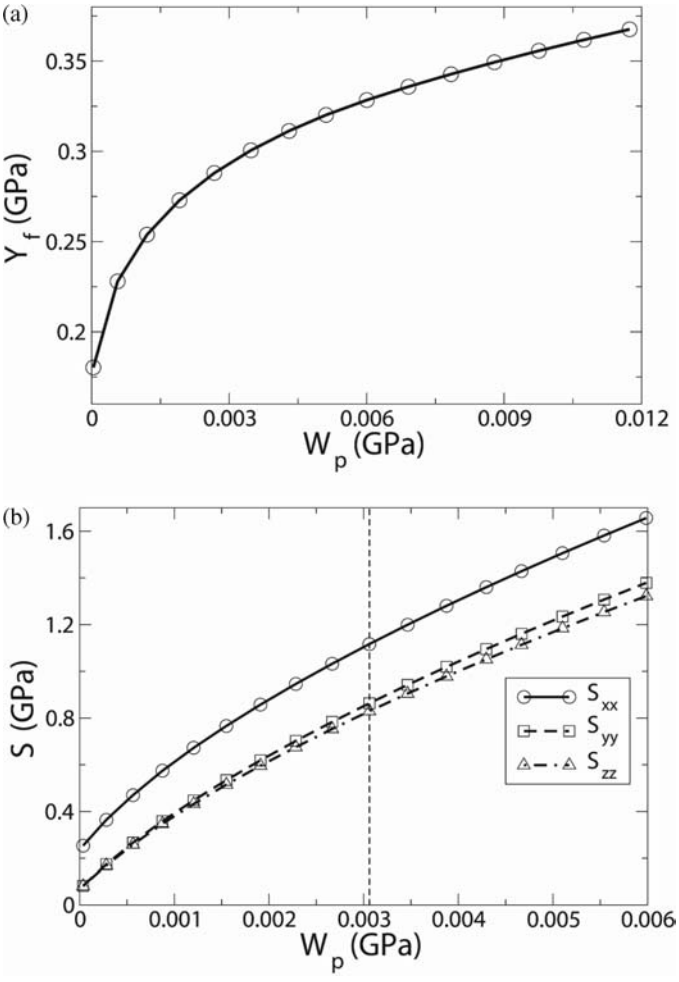

FIG. 12. (a) Yield stress as a function of macroscopic plastic work; (b) macroscopic stresses as functions of macroscopic plastic work.

represented by various macroscopic strain combinations, $e_{xx} : e_{yy} : e_{xy} = 1 : a : b$, where $a = 0, 0.5, 1.0$ and 2.0, and $b = 0, 0.5, 1.0$ and 2.0, respectively. A total of 16 numerical experiments are performed, and macroscopic stresses and plastic work are obtained for each case in the principal axes of anisotropy from equations (28). For each loading condition, macroscopic stresses in principal axes of anisotropy are plotted as functions of plastic work W_p, as shown in Figure 12(b).

(ii) Assuming that the plastic work (W_p) is invariant with respect to the loading condition. For a given value of macroscopic plastic work, yield stress $Y_f(W_p)$ is obtained from the curve plotted in section 4.2.1, macroscopic stresses components for each loading conditions are obtained from the curves plotted in step (i), as shown in Figure 12(b). Then anisotropic parameters *F, G* and *H* in yield criterion (26) are evaluated by minimizing the function $\sum_{i=1}^{16} \phi_i^2(F, G, H)$ using least square method for this macroscopic plastic work for the 16 numerical experiments. This step is repeated for different values of macroscopic plastic work and the anisotropic parameters are plotted as functions of W_p.

4.2.3. Parameters Q_1, Q_a, Q_b and Q_c

(i) A macro-micro pure shear problem is solved with RVE homogenization while the matrix material has non-zero initial void volume fraction. The macroscopic stresses and averaged void volume fraction are plotted as functions of W_p, where the averaged incremental plastic work is $\dot{W}_p = \frac{1}{\Omega}\int_\Omega \frac{1}{1-f}\sigma_{ij}\dot{\varepsilon}_{ij}^p d\Omega$. Because normal stresses equal to zero and void volume fraction does not change, Q_1 can be determined directly by solving the following yield equation with different Σ_{xy} and corresponding Y_f.

$$\frac{3\Sigma_{xy}^2}{Y_f^2} + 2Q_1 f - \left(1 + Q_1^2 f^2\right) = 0$$

(ii) The same set of numerical experiments used in section 4.2.2 for the RVE is again performed for the matrix material with non-zero initial void volume fraction.

(iii) Again, assuming that the plastic work is invariant with the loading condition, the parameters Q_a, Q_b and Q_c in yield criterion (23) are evaluated by minimizing the function $\sum_{i=1}^{16} \phi_i^2(Q_a, Q_b, Q_c)$ using least square method with calibrated anisotropic parameters *F, G* and *H*. This step is repeated for different values of macroscopic plastic work and subsequently, the parameters Q_a, Q_b and Q_c are plotted as functions of W_p.

4.3. Numerical Implementation

The macroscopic constitutive laws for the ductile material consisting of brittle particles and undergoing ductile failure are derived from the anisotropic yield function (24) with associated flow rule and strain hardening. In an incremental form, the macroscopic stress increments $\Delta\Sigma_{ij}$ are related to increments of strains as

$$\Delta\Sigma_{ij} = E_{ijkl}\left(\Delta e_{kl} - \Delta e_{kl}^p\right) \tag{29}$$

where E_{ijkl} is the homogenized elastic tensor. Using associated flow rule, the components of plastic strain increment are obtained as:

$$\Delta e_{xx}^p = \Delta\lambda\frac{\partial\phi}{\partial\Sigma_{xx}}, \quad \Delta e_{yy}^p = \Delta\lambda\frac{\partial\phi}{\partial\Sigma_{yy}},$$
$$\Delta e_{xy}^p = \Delta\lambda\frac{\partial\phi}{\partial\Sigma_{xy}} \quad \Delta e_{zz}^p = \Delta\lambda\frac{\partial\phi}{\partial\Sigma_{zz}} \tag{30}$$

Elimination of the flow parameter $\Delta\lambda$ from equations (24) results

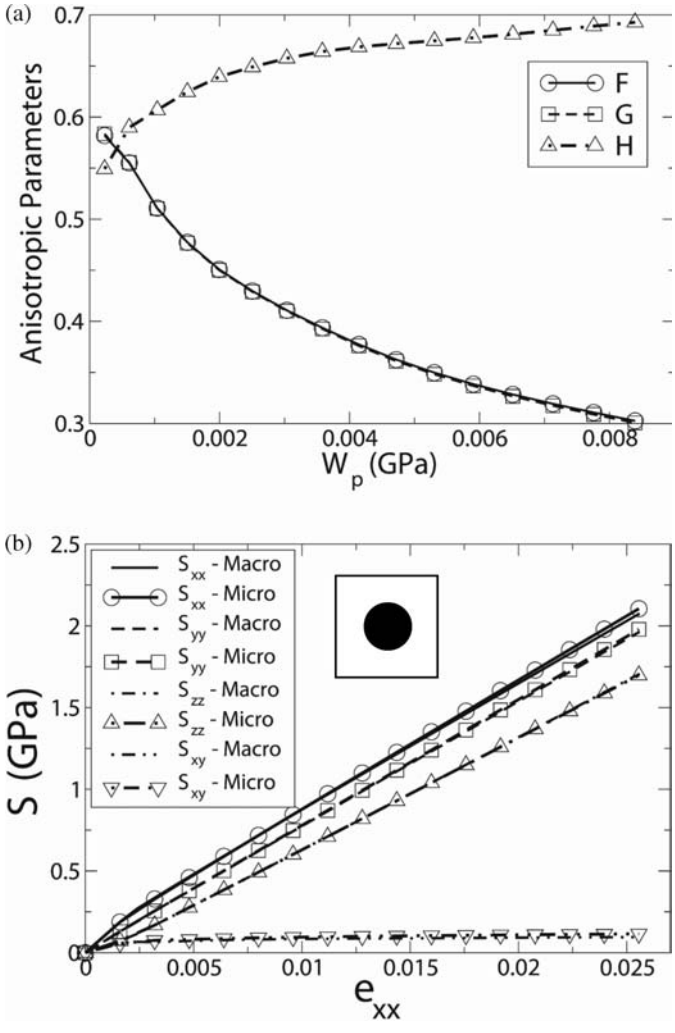

FIG. 13. (a) Anisotropic plastic yield parameters; (b) comparison of strain-stress response by the macroscopic constitutive model with that by microscopic RVE analysis with homogenization for a simple unit cell with one particle.

in the set of equations

$$\begin{aligned}
\Delta e^p_{xx}\left(\frac{\partial\phi}{\partial\Sigma_{yy}}\right) - \Delta e^p_{yy}\left(\frac{\partial\phi}{\partial\Sigma_{xx}}\right) &= 0,\\
\Delta e^p_{xx}\left(\frac{\partial\phi}{\partial\Sigma_{xy}}\right) - \Delta e^p_{xy}\left(\frac{\partial\phi}{\partial\Sigma_{xx}}\right) &= 0,\\
\Delta e^p_{xx}\left(\frac{\partial\phi}{\partial\Sigma_{zz}}\right) - \Delta e^p_{zz}\left(\frac{\partial\phi}{\partial\Sigma_{xx}}\right) &= 0
\end{aligned} \tag{31}$$

With known increments of strain, the set of equation (31), together with the yield function equation (24), are solved iteratively by using the Newton-Raphson method to obtain stress increments using the following steps.

(i) Initialize values of $\Delta\Sigma_{xx}$, $\Delta\Sigma_{yy}$, $\Delta\Sigma_{zz}$ and $\Delta\Sigma_{xy}$ by using $\Delta\Sigma_{ij} = E_{ijkl}\Delta e_{kl}$

(ii) Calculate the gradient $(\frac{\partial\phi}{\partial\Sigma_{ij}})$ of yield function and solve for the increments of plastic strain Δe^p_{xx}, Δe^p_{yy}, Δe^p_{zz}andΔe^p_{xy} from equations (31) and (24). Update the stresses, void volume fraction and plastic work using the relation

$$\Delta W_p = \Sigma_{xx}\Delta e^p_{xx} + \Sigma_{yy}\Delta e^p_{yy} + \Sigma_{zz}\Delta e^p_{zz} + \Sigma_{xy}\Delta e^p_{xy} \tag{32}$$

(iii) Update all parameters using the updated plastic work.

(iv) If $\phi \le tol_1$ and correction to plastic strain increment $\delta e^p_{ij} \le tol_2$, where tol_1, tol_2 are prescribed tolerances, then stop. Otherwise go to step (ii).

4.4. Numerical Examples

The homogenized anisotropic GTN model is validated by comparing the results of a range of macroscopic numerical simulations with those obtained by coupled macro-micro scale analysis using LE-VCFEM and homogenization. Simulations are conducted for two heterogeneous microstructures, without

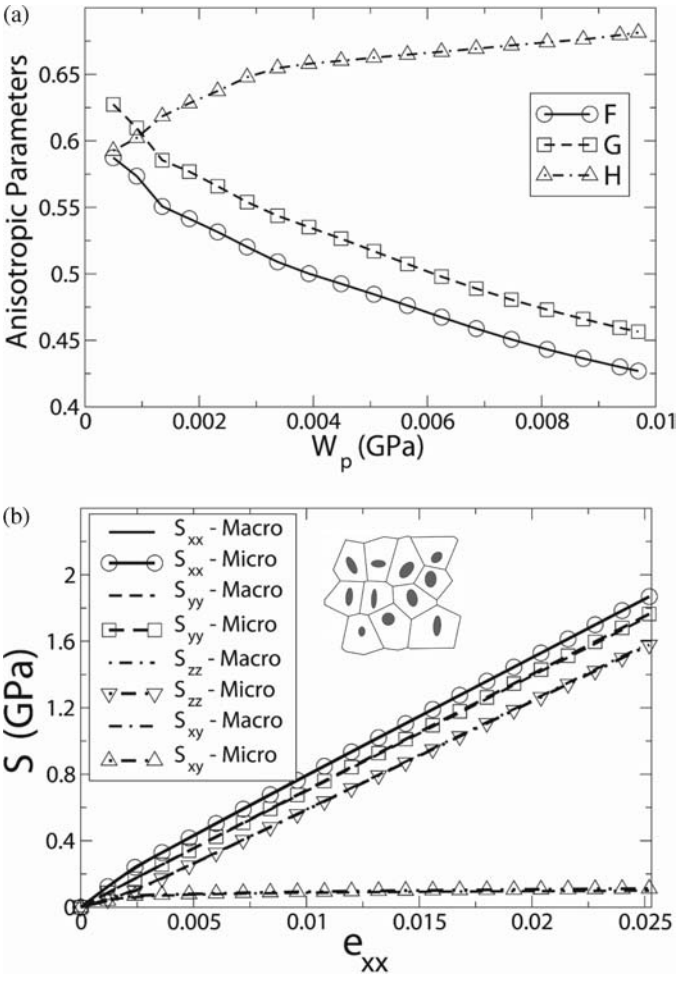

FIG. 14. (a) Anisotropic plastic yield parameters; (b) comparison of strain-stress response by the macroscopic constitutive model with that by microscopic RVE analysis with homogenization for an arbitrary RVE with 11 random distributed particles.

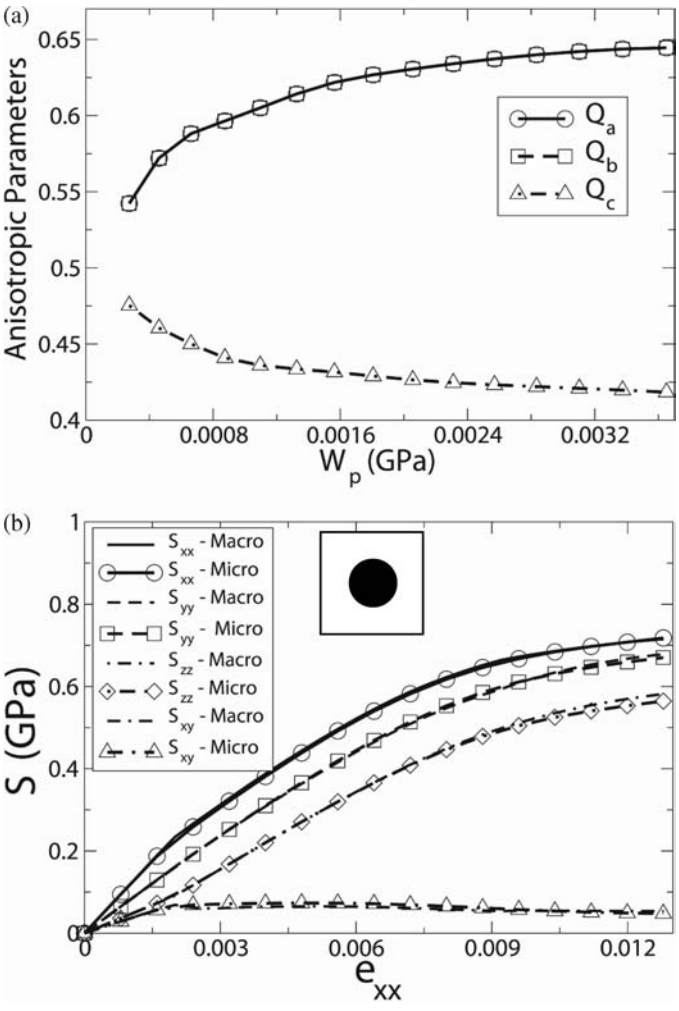

FIG. 15. (a) Anisotropic parameters for the hydrostatic portion of plastic yield; (b) comparison of strain-stress response by the macroscopic constitutive model with that by microscopic RVE analysis with homogenization for a simple unit cell with one particle.

and with voids. The RVEs considered are: (1) a square matrix domain with one circular particle and (b) an arbitrary shaped domain with 11 randomly distributed particles of different sizes and shapes (Figure 11). The RVE material properties for the matrix are $E = 66\,\text{GPa}$, $v = 0.33$. The post yield behavior for the pure matrix material without voids is expressed by the Ramberg-Osgood law ($\sigma_m = \sigma_0(\frac{\varepsilon_m^p}{\alpha\varepsilon_0})^{\frac{1}{n}}$), where the initial flow stress of the matrix is $\sigma_0 = 440\,\text{MPa}$, ε_0 is the strain at yield ($\varepsilon_0 = \sigma_0/E$), material parameter $\alpha = 3/7$ and strain hardening exponent $n = 12.5$. For the brittle particles, $E = 400\,\text{GPa}$ and $v = 0.2$.

4.4.1. *Simulations with the Anisotropic Plasticity Model for Microstructure Without Voids*

Anisotropic parameters for the two RVE's are plotted in Figures 13(a) and 14(a) as functions of W_p. Results of a pure macroscopic analysis using the anisotropic plasticity model of equations (24, 25, 29, 30) are compared with pure micromechanics based results that are averaged after each load step. The results of this comparison for the loading condition ($e_{xx} : e_{yy} : e_{xy} = 4 : 2 : 3$) are shown in Figures 13(b) and 14(b) with good agreement. Comparisons for other loading conditions represented by various strain combinations (not shown) also show good agreement.

4.4.2. *Simulations with the Anisotropic Plasticity-damage Model for Microstructure with Voids*

The same simulations of section 3.4.1 are revisited for the two RVE's, now with 0.1% initial void volume fraction. The calibrated parameter Q_1 shows that it doesn't change with plastic work for both RVEs, $Q_1 = 1.5$. The evolutions of parameters Q_a, Q_b and Q_c with W_p are shown in Figures 15(a) and 16(a). Results of simulations by the anisotropic ductile damage model are compared with those by micromechanical RVE analysis with homogenization under the loading condition ($e_{xx} : e_{yy} : e_{xy} = 4 : 2 : 3$) in Figures 15(b) and 16(b). The results show good agreement. Additional calibrations and simulations are done for the RVE with 2 aligned long particles. Comparisons are shown in Figure 17.

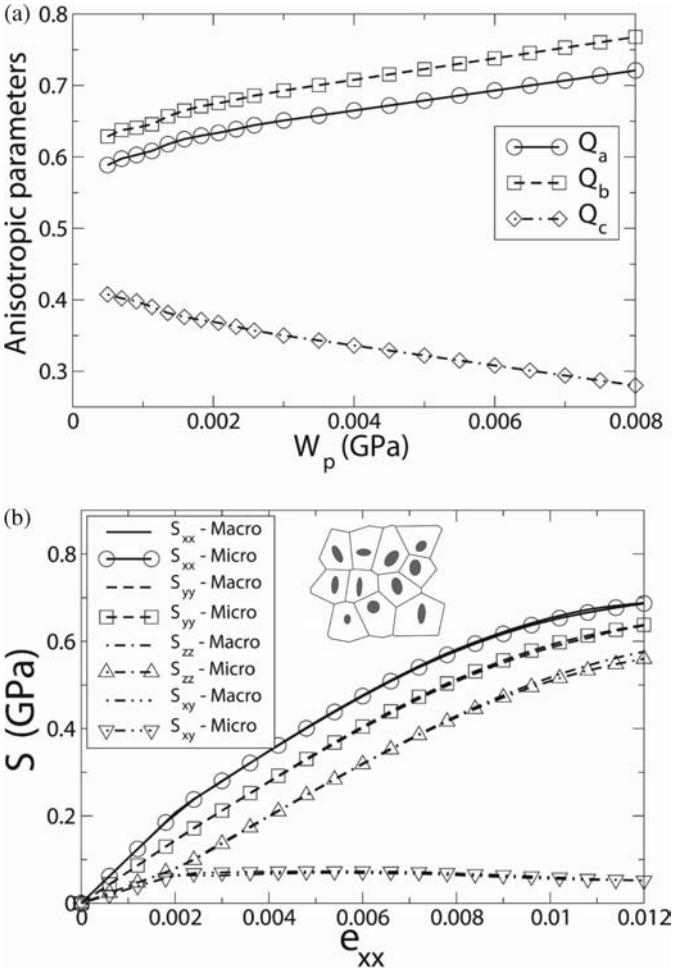

FIG. 16. (a) Anisotropy parameters for the hydrostatic portion of plastic yield; (b) comparison of strain-stress response by the macroscopic constitutive model with that by microscopic RVE analysis with homogenization for an arbitrary RVE with 11 random distributed particles.

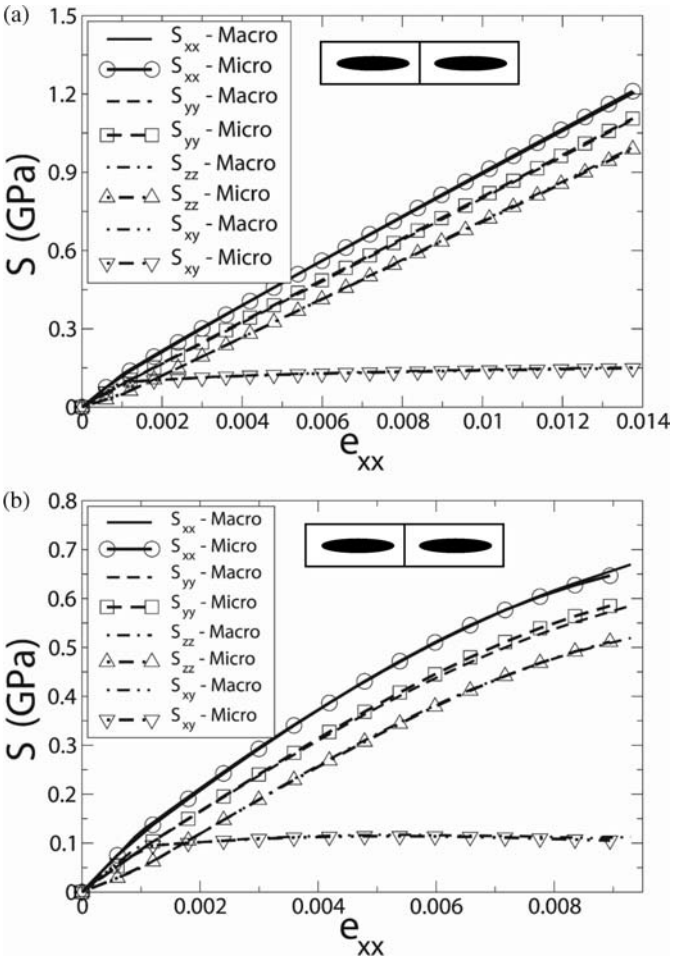

FIG. 17. Comparison of strain-stress response by the macroscopic constitutive model with that by microscopic RVE analysis with homogenization for RVE with 2 aligned particles (a) without voids; (b) with voids.

5. CONCLUSIONS

This paper develops three modules contributing to the overall framework of multi-scale modeling of ductile fracture of particle reinforced metallic materials, e.g., cast aluminum alloys with dispersed particulates. The first module introduces a morphology based domain partitioning (MDP) as a preprocessor to multiscale modeling, identifying regions of strong inhomogeneity in the microstructural domain. The three step simulation-characterization-partitioning technique provides a delineation of various length scales in the microstructure.

The second module is for detailed micromechanical analysis of particle fragmentation and matrix cracking of heterogeneous microstructures leading to ductile fracture. This module is necessary for RVE level analysis with periodicity (level-1) as well as pure micromechanical analysis in regions where periodicity ceases to hold (level-2) in the multi-level analysis discussed in [16, 17, 50]. The Voronoi cell FEM for particle fragmentation is extended in this paper to incorporate ductile failure through matrix cracking in the form of void growth and coalescence using a non-local Gurson-Tvergaard-Needleman (GTN) model. In the resulting locally enriched VCFEM or LE-VCFEM, the assumed stress-based hybrid VCFEM formulation is overlaid with narrow bands of displacement based elements to accommodate strain softening in the constitutive behavior. Numerical examples presented show the potential of LE-VCFEM in accurate microstructural modeling of ductile fracture.

The third module in this paper develops a homogenized anisotropic plasticity-damage model for macroscopic analysis in the multi-scale material model. The anisotropic model is taken to be in the form of the GTN model. Parameters in this model are calibrated from results of homogenization of microstructural variables obtained by LE-VCFEM analysis of microstructural RVE containing particles, matrix and voids. Numerical examples are simulated with this model for different RVE's undergoing a wide variety of load paths. Comparison between the anisotropic GTN model and homogenized micromechanics results shows excellent agreement. Thus the model is suitable for being implemented in macroscopic finite element codes [51] to represent ductile failure in composites as long as the basic RVE assumptions remain valid. The authors are currently working on integrating these modules in a comprehensive multi-scale framework, which will be reported in subsequent papers.

REFERENCES

1. Q.C. Wang, C.H. Caceres, J.R. Griffiths, Jr., Damage by Eutectic Particle Cracking in Aluminum Casting Alloys A356/357, Metall. Mater. Trans. A., vol. 34A, pp. 2901–2912, 2003.
2. Q.C. Wang, Microstructural Effects on the Tensile and Fracture Behavior of Aluminum Casting Alloys A356/357, Metall. Mater. Trans. A., vol. 34A, pp. 2887–2899, 2003.
3. J.M. Boileau, The Effect of Solidification Time on the Mechanical Properties of a Cast 319 Aluminum Alloy, Ph.D. Dissertation, Wayne State University, 2000.
4. W.J. Poole, E.J. Dowdle, Experimental Measurements of Damage Evolution in Al-Si Eutectic Alloys, Scripta Mater., vol. 39, pp. 1281–1287, 1998.
5. A.S. Argon, J. Im, R. Sofoglu, Cavity Formation from Inclusions in Ductile Fracture, Metall. Mater. Trans. A., vol. 6A, pp. 825–837, 1975.
6. C.H. Caceres, Particle Cracking and the Tensile Ductility of a Model Al-Si-Mg Composite System, Aluminum Transactions, vol. 1, pp. 1–13, 1999.
7. C.H. Caceres, J.R. Griffiths, Damage by the Cracking of Silicon Particles in an Al-7Si-0.4Mg Casting Alloy, Acta Mater., vol. 44, pp. 25–33, 1996.
8. T. Christman, T. Needleman, S. Suresh, An Experimental and Numerical Study of Deformation in Metal-Ceramic Composites, Acta Metall. et Mater. vol. 37, pp. 3029–3050, 1989.
9. C. Gonzalez, J. Llorca, Prediction of the Tensile Stress-Strain Curve and Ductility in Al/SiC Composites, Scripta Metall., vol. 35(1), pp. 91–97, 1996.
10. E. Weissenbek, H.J. Boehm, F.G. Rammerstoffer, Micromechanical Investigations of Fiber Arrangement Effects in Particle Reinforced Metal Matrix Composites, Comp. Mater. Sci., vol. 3, pp. 263–278, 1994.
11. S. Ghosh, Y. Ling, B. Majumdar, R. Kim, Interfacial Debonding Analysis in Multiple Fiber Reinforced Composites, Mech. Mater., vol. 32, pp. 561–591, 2000.
12. M. Li, S. Ghosh, O. Richmond, An Experimental-Computational Approach to the Investigation of Damage Evolution in Discontinuously Reinforced Aluminum Matrix Composites, Acta Mater., vol. 47(12), pp. 3515–3552, 1999.
13. S. Ghosh, S. Moorthy, Particle Fracture Simulation in Non-Uniform Microstructures of Metal-Matrix Composites, Acta Mater., vol. 46, pp. 965–982, 1998.
14. S. Moorthy, S. Ghosh, A Voronoi Cell Finite Element Model for Particle Cracking in Elastic-Plastic Composite Materials, Comput. Meth. Appl. Mech. Engrg., vol. 151, pp. 377–400, 1998.
15. S. Li, S. Ghosh, Debonding in Composite Microstructures with Morphological Variations, Int. Jour. Comput. Methods, vol. 1, no. 1, pp. 121–149, 2004.
16. S. Ghosh, K. Lee, P. Raghavan, A Multi-Level Computational Model for Multiscale Damage Analysis in Composite and Porous Materials, Int. J. of Solids Struct. vol. 38, no. 14, pp. 2335–2385, 2001.
17. P. Raghavan, S. Ghosh, Adaptive Multi-Scale Computational Modeling of Composite Materials, Comp. Model. Engrg. Sci., vol. 5, pp. 151–170, 2004.
18. S. Ghosh, D.M. Valiveti, S.H. Harris, J. Boileau, Microstructure Characterization Based Domain Partitioning as a Pre-Processor to Multi-Scale Modeling of Cast Aluminum Alloys, Model. Simul. Mater. Sci. Engrg., vol. 14, pp. 1363–1396, 2006.
19. D.M. Valiveti, S. Ghosh, Domain Partitioning of Multi-Phase Materials Based on Multi-Scale Characterizations: A Preprocessor for Multi-Scale Modeling, Int. Jour. Numer. Meth, Engrg., vol. 69(8), pp. 1717–1754, 2007.
20. A.K. Ghosal, R. Narasimhan, Mixed-Node Fracture Initiation in a Ductile Material with a Dual Population of Second-Phase Particles, Mater. Sci. Engrg., vol. A211, pp. 117–127, 1996.
21. D. Steglich, W. Brocks, Micromechanical Modeling of the Behavior of Ductile Materials Including Particles, Comput Mater Sci, vol. 9, pp. 7–17, 1997.
22. J. Llorca, C. Gonzalez, Microstructural Factors Controlling the Strength and Ductility of Particle Reinforced Metal-Matrix Composites, J. Mech. Phys. Solids, vol. 46, pp. 1–28, 1998.
23. J.B. Leblond, G. Perrin, J. Devaux, Bifurcation Effects in Ductile Metals with Nonlocal Damage, J. Appl. Mech., vol. 61, pp. 236–242, 1994.
24. V. Tvergaard, A. Needleman, Effect of Non-Local Damage in Porous Plastic Solids, Int. J. of Solids. Struct., vol. 32, pp. 1063–1077, 1995.
25. V. Tvergaard, A. Needleman, Nonlocal Effects on Localization in a Void-Sheet, Int. J. of Solids Struct., vol. 34, pp. 2221–2238, 1997.
26. J.R. Rice, The Localization of Plastic Deformation, Proc. 14th Int. Congr. On Theoretical and Applied Mechanics, Delft, Amsterdam, pp. 207–20, North-Holland, New York, 1976.

27. W.Y. Chien, J. Pan, S.C. Tang, Modified Anisotropic Gurson Yield Criterion for Porous Ductile Sheet Metals, J Engrg Mater Tech, vol. 123, pp. 409–416, 2001.
28. A.A. Benzerga, J. Besson, A. Pineau, Anisotropic Ductile Fracture, Part II: Theory, Acta Mater., vol. 52, pp. 4639–4650, 2004.
29. A.A. Benzerga, J. Besson, Plastic Potential for Anisotropic Porous Solids, Eur J Mech, vol. 20A, pp. 397–434, 2001.
30. A.A. Benzerga, J. Besson, R. Batisse, A. Pineau, Synergistic Effects of Plastic Anisotropy and Void Coalescence on Fracture Mode in Plane Strain, Modeling Simul Mater Sci Eng, vol. 10, pp. 73–102, 2002.
31. A.M. Gokhale, S. Yang, Application of Image Processing for Simulation of Mechanical Response of Multi-Length Scale Microstructures of Engineering Alloys, Metall. Mater. Trans, vol. A30, pp. 2369–81, 1999.
32. A. Tewari, A.M. Gokhale, J.E. Spowart, D.B. Miracle, Quantitative Characterization of Spatial Clustering in Three-Dimensional Microstructures Using Two-Point Correlation Functions, Acta Materialia, vol. 52, pp. 307–19, 2004.
33. C.L.Y. Yeong, S. Torquato, Reconstructing Random Media, Phys. Rev. E, vol. 57, pp. 495–505, 1998.
34. M.D. Rintoul, S. Torquato, Reconstruction of Structure of Dispersions, Jnl. of Colloid and Interface Science, vol. 186, pp. 467–76, 1997.
35. D.W. Cooper, Random Sequential Packing Simulation in Three Dimensions for Spheres, Phys. Rev. A, vol. A38, pp. 522–24, 1998.
36. R.K. Everett, J.H. Chu, Modeling of Non-Uniform Composite Microstructures, J. Compos. Mater, vol. 27, pp. 1128–44, 1992.
37. R. Everson, L. Sirovich, K.R. Sreenivasan, Wavelet Analysis of the Turbulent Jet, Physics Letters A, vol. 145, pp. 314–22, 1990.
38. L. Prasad, S.S. Iyengar, Wavelet Analysis with Applications to Image Processing, CRC Press, Boca Raton, FL, 1997.
39. S. Torquato, Random Heterogeneous Materials: Microstructure and Macroscopic Properties, Springer-Verlag New York, 2002.
40. C.H. Caceres, J.R. Griffiths, P. Reiner, The Influence of Microstructure on the Bauschinger Effect in An Al-Si-Mg Casting Alloy, Acta Mater., vol. 44, pp. 15–23, 1996.
41. J.E. Spowart, B. Maruyama, D.B. Miracle, Multiscale Characterization of Spatially Heterogeneous Systems: Implications for Discontinuously Reinforced Metal-Matrix Composite Microstructures, Mat. Sci. Engrg., vol. A307, pp. 51–66, 2001.
42. N. Aravas, On the Numerical Integration of a Class of Pressure-Dependent Plasticity Models, Int. J. Numer. Meth. Engrg., vol. 24, pp. 1395–1416, 1987.
43. J.M. Bass, J.T. Oden, Adaptive Finite Element Methods for a Class of Evolution Problems in Visco-Plasticity, Int. J. Engrg Sci, vol. 6, pp. 623–653, 1987.
44. T.J.R. Hughes, Generalization of Selected Integration Procedures to Anisotropic and Nonlinear Media, Int. J. Number Methods Engrg., vol. 15, pp. 1413–1418, 1980.
45. S. Ghosh, N. Kikuchi, An arbitrary Lagrangian-Eulerian Finite Element Method for Large Deformation Analysis of Elastic-Viscoplastic Solids, Comput. Methods Appl. Mech. Engrg., vol. 86, pp. 127–188, 1991.
46. C.C. Chu, A. Needleman, Void Nucleation Effects in Biaxially Stretched Sheets, J. Eng. Mater. Tech., vol. 102, pp. 249–256, 1980.
47. V. Tvergaard, Influence of Voids on Shear Band Instabilities Under Plane Strain Conditions, Int. J. Fract. Mech., vol. 17, pp. 389–407, 1981.
48. O.C. Zienkiewicz, J.Z. Zhu, The Super-Convergent Patch Recovery and a Posteriori Error Estimates. Part 1: The Recovery Technique, Int. J. Numer. Methods Eng., vol. 33, pp. 1331–1364, 1992.
49. R.A. Hill, A Theory of Yielding and Plastic Flow of Anisotropic Metals, Proc. Roy. Soc. London, Ser. A., vol. 193, pp. 281–297, 1948.
50. P. Raghavan, S. Ghosh, Concurrent Multi-Scale Analysis of Elastic Composites by a Multi-Level Computational Model, Comp. Meth. Appl. Mech. Engrg., vol. 193, pp. 497–538, 2004.
51. K.S. Surana, A. Rajwani, J.N. Reddy, The k-version Finite Element Method for Singular Boundary-Value Problems with Application to Linear Fracture Mechanics, International Journal for Computational Methods in Engineering Science and Mechanics, vol. 7 (3), pp. 217–239, 2006.